

Author's Response to the Referee Comments

Manuel Gutleben, Silke Groß, Martin Wirth and Bernhard Mayer

September 1, 2020

The authors would like to thank the referees very much for carefully reading the submitted manuscript and for their helpful and very valuable suggestions and feedbacks. In the following, all comments and questions will be addressed and answered. The comments are repeated and a direct response is given below. In addition, changes in the manuscript are highlighted in the appended marked-up manuscript version using blue (additions) and red (removals) colors.

Reply to Minor Comments of Referee #2 on 11 June 2020

Main points

(I) A clear definition of the term '*marine boundary layer*' (MBL) is missing. In the presented case studies (Fig. 4) the so-called MBL reaches up to the trade wind inversion at about 1.4-1.8 km height. Later, it is stated that the SAL is confined at the bottom by the trade wind inversion which is not in line with the indicated SAL in Fig. 4. Please explain in a more quantitative way how the upper limit of the MBL and the lower limit of the SAL are determined in your study. Various attempts to describe the vertical stratification in the Caribbean are found in literature ('convective marine boundary layer (CMBL)' in Groß et al. (2016), 'sub-cloud layer (SCL)' and 'intermediate layer (IL)' in Jung et al. (2013), 'marine aerosol layer (MAL)' in Rittmeister et al. (2017)). The convective part (CMBL or SCL) of the MBL or MAL is clearly visible in Fig. 2 and reaches up to around 600 m height. A definition of the MBL as used in the present study would improve the manuscript.

Thank you for this valuable feedback. In literature one can find many definitions to partitions of vertical atmospheric profiles in regions impacted by SALs (Figure 1).

Rittmeister et al. (2017) for example, define the so-called MAL (Marine Aerosol Layer) as the layer which reaches from ground-level to the SAL-bottom. In their study they also state that the SAL bottom is equal to the trade wind inversion (TWI). This may be the case for their shipborne lidar observations, but it is certainly not the case for our observations. During NARVAL-II the TWI and the SAL-base differed, as the SAL was often observed to be a decoupled layer which penetrated into the free troposphere (with its own inversions at the top and the bottom). Our measurements indicate three inversions in dust-laden regions (the TWI and two additional ones at the SAL base and the SAL top).

Jung et al. (2013) divide the region below the SAL into a sub-cloud layer (reaching to approximately 500-600 m altitude) and an intermediate layer (IL) that reaches from the SCL top to the SAL bottom. Like Rittmeister et al. (2017) they also identify the SAL base to represent the TWI.

Another approach to characterize the vertical domain below the SAL is performed by Groß et al. (2016). In cloud-free regions they define a convective boundary layer (CMBL) which is confined by strong gradients in particle backscatter, depolarization and potential temperature. In case of a cloudy lower troposphere, the CMBL equals the so-called sub-cloud layer (SCL) and is topped by a cloud layer (CL). The CL itself is confined by an inversion layer.

The dropsonde and lidar analysis presented in Gutleben et al. (2019) partially follows the definitions made by Groß et al. (2016). In their paper the SAL-impacted atmosphere is divided into three regimes:

1. a Marine Boundary Layer (MBL): it is confined by the TWI which is characterized by a rapid temperature decrease and a strong hydrolapse,
2. the Saharan Air Layer (SAL), which is confined by two inversions at the bottom and the top. While the lower inversion is caused by the strong vertical gradients of temperature between the hot SAL-base

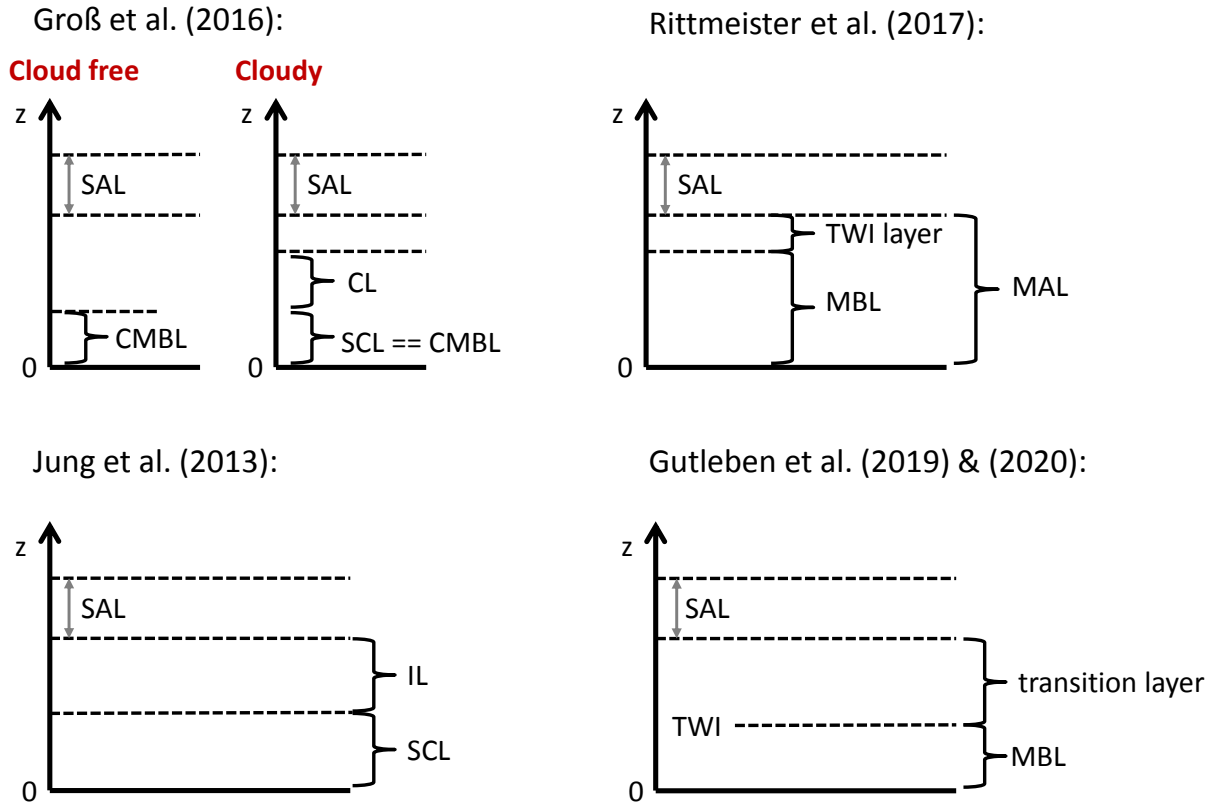


Figure 1: Illustration of definitions to partitions of vertical atmospheric profiles in regions impacted by SALs as found in literature.

and the subjacent cooler marine air below (Prospero and Carlson, 1972; Dunion and Velden, 2004), the upper inversion forms due to the predominant large-scale subtropical subsidence in the upper troposphere (Gamo, 1996).

3. a transition or mixed layer between the MBL and the SAL.

- 5 As described in Groß et al. (2016), the MBL described in Gutleben et al. (2019) is additionally divided into a sub-cloud layer which extends from the ocean surface to approximately 0.5 to 0.7 km altitude and a cloud layer which extends from the sub-cloud layer top to the TWI. Whereas the sub-cloud layer is well mixed (constant water vapor mixing ratio and constant potential temperature), the cloud layer shows a conditionally unstable lapse rate.
- 10 In this paper we follow the definitions made in Gutleben et al. (2019) for the definition of the MBL. They seem to be most appropriate for the observations during NARVAL-II. However, we are aware that a clear description in the submitted manuscript was missing. This is why we added the following paragraph in the revised manuscript:

Additionally the extent of the lowest atmospheric layer - the marine boundary layer (MBL) - can be determined. It covers the lowest couple of kilometers in a marine atmosphere. The MBL represents a well mixed layer that is characterized by high humidity. As the MBL is confined by the TWI, its upper limit is coming along with a strong increase of potential temperature and a pronounced hydrolapse (Gutleben et al., 2019). By searching for those features in measured profiles of r_m (DIAL) and Θ (dropsondes), an approximation of the vertical extent of the MBL is additionally outlined.

20

(II) Some comments concerning the aerosol classification (Sec. 2.4.1): You discuss only the contribution of pure mineral dust and pure marine aerosol and its mixture. What about contributions of other aerosol types like pollution from the African continent? At this time of the year, it is not very likely, but should be mentioned. The effect of dry marine aerosol on the depolarization ratio was even studied at Barbados and is described in Haarig et al. (2017a).

Thank you for this comment. As you already mentioned, the NARVAL-II campaign took place in summer 2016. This time of the year marks the off-season of transatlantic transport of biomass-burning aerosols. No evidence of the transport of biomass burning aerosols towards the Caribbean was found by looking at MODIS imagery along the SAL backward trajectory. Moreover, the particle linear depolarization ratio inside the SAL would decrease significantly with biomass burning aerosols present (e.g. Groß et al., 2013). To clarify this issue we mentioned that no biomass burning aerosols were evident during NARVAL-II in the revised manuscript:

Other aerosol types, like e.g. African biomass burning aerosols, are also not expected in the measurement region and no evidence for such types was found across the subtropical North Atlantic Ocean by looking at satellite imagery.

Moreover, we added the study by Haarig et al. (2017a) on dry marine aerosol depolarization to the discussion why no dry marine aerosol is expected at low atmospheric levels. We cited the paper and appended it to the list of references.

(III) Some comments concerning Section 2.4.2: The lidar ratios for dust (47 sr) and marine aerosol (18 sr) are based on literature from different locations around the globe. However, Groß et al., 2015, reported higher dust lidar ratios of 56 ± 7 sr for Barbados. Could you derive with your high spectral resolution lidar (HSRL) actual lidar ratios of the pure types during your campaign to judge which lidar ratios are more appropriate for your situation? What values for the particle linear depolarization ratio have you used in Eq. 4 and 5? 0.26 and 0.04? From the text it is not clear whether you have calculated the conversion factors (extinction to volume) using the method described in Mamouri and Ansmann (2016) or whether you have taken the values from the literature. Looking into the cited paper, I can't find your conversion factors.

We followed your suggestion and had a look on the measured lidar ratios during NARVAL-II. We found that the lidar ratios inside dust layers are indeed taking values around 47 sr, and are by far not as high as the presented values by Groß et al. (2015). The differences may arise from the two different measurement methods (Raman in Groß et al. (2015) compared to HSRL in this study). Nevertheless, even if higher lidar ratios for the calculation of the dust-contribution to the total extinction coefficient were used, they would not have a significant impact on the presented results.

The used particle linear depolarization ratios for the conversions are 0.04 for marine aerosol and 0.26 for mineral dust aerosol. We added the information to the revised manuscript.

Thank you for your very useful comment on the used conversion factors. We erroneously mentioned a marine aerosol conversion factor that has not been used for calculations in the submitted manuscript. We used it in a very first approach one or two years ago, before we found out that it is wrong. Both used correct conversion factors for marine and mineral dust aerosol in the submitted study are taken from the study by Groß et al. (2016). In their study they compared in-situ measurements of particle mass concentrations over Barbados to concentrations derived by lidar measurements using conversion factors. They found a good agreement. The used conversion factors are given on page 11538 - chapter 2.7: 0.66×10^{-6} m for marine aerosol and 0.65×10^{-6} m for transported mineral dust. We are very sorry for the confusion and corrected the factor in the revised manuscript.

(IV) For your radiative transfer calculations, it is important that no cirrus cloud is present above the scene. The upper panel of Fig. 1 (not yet used in the text) supports the absence of cirrus clouds.

You are absolutely right. Cirrus clouds would have a major impact on calculated radiative effects and heating rates. We double-checked that issue by looking at MODIS satellite imagery and photos made on-board the HALO aircraft during that flight. As mentioned at the very beginning of Section 3 (Px L09) we took cloudless 5-min-lidar cross sections for calculations. To clarify that the wording 'cloudless' also implies that no cirrus clouds have been present above the lidar scenes, we added the following sentence to the revised manuscript: *Here, MODIS imagery of the respective regions is additionally used to ensure that that no cirrus clouds have been present above the observed lidar scenes.*

Minor points

1. **Comment: Pii, L12 + L26: Using the term 'we' for studies by the same authors is a matter of taste.**

5 We changed *we* to *they*.

2. **Comment: Pii, L21: Gutleben et al. (2019x), x = a or b**

We corrected that.

10 3. **Comment: Pii, L 6: Haarig et al. (2018), describes smoke, you probably mean Haarig et al. (2017b)**

You are right. We corrected this incorrect citation.

4. **Comment: Piv, Eq (1) What is $\delta T/\delta t$? And two lines later a δ is missing (δF)**

15 We corrected the mistakes.

5. **Comment: Pv, L8: Saharan dust *and* marine aerosols**

We added *and*.

20 6. **Comment: Pv, L11: Burton et al. (2012), is not a good reference for the unchanged dust properties. It describes the aerosol classification and gives just a case study showing mineral dust. Look for other references.**

We removed this citation from the manuscript.

25 7. **Comment: Pvi, Eq (2)(5) and the whole page: Indices should not be written in italic.**

We changed that.

8. **Comment: Pvii, Table 2: The percentages for the mixing ratio refer to which quantity (volume, number,...)?**

30 Shown percentages refer to mass mixing ratios. We added that information.

9. **Comment: Pix, Fig. 2, caption: The profiles are not shown in red and blue, but green and black.**

We corrected the text in the figure caption.

35 10. **Comment: Fig. 2 and Pxi, case (a): There is still a thin layer of some depolarizing particles between 1.7 and 2.5 km height. You are right, there are no dust signatures above 3 km height. But what about the particles above the MBL top? Please discuss this issue shortly.**

40 We added two sentences to discuss this issue: *Above the MBL some signatures of depolarizing particles ($\delta_{p(532)} < 0.25$) with weak backscatter can be identified. Those signatures are most likely caused by settling dust particles from the dissipating SAL nearby (see Figure 1).*

11. **Comment: Fig. 3, caption: light-green \rightarrow light-blue**

We corrected the description of the color in the caption.

45 12. **Comment: Pxi, L27/28: 'Case (a) however, indicates that no distinct correlation of enhanced r_m and R_{532} could be observed in a SAL-free troposphere.' What do you mean by 'no distinct correlation'? Both curves are decreasing with height.**

50 We removed this confusing sentence and changed it to: *Measured profiles of r_m and $R_{(532)}$ for case (a), show that no enhanced water vapor concentrations could be observed in the SAL-free troposphere. The water vapor profile shows a drop of r_m to values smaller 1 g kg^{-1} at altitudes greater 3 km, indicating the transition from the MBL to the dry free troposphere.*

13. **Comment: Pxii, L5: 24 h-averaged** The explanation follows some pages later: 'It is assumed that the observed profiles do not change and remain stationary within a 24 h time frame.' (Pxiv) Here, '24 h-averaged' clarifies that heating rates are averaged over a whole day and are given in units Kd^{-1} . However, the description that the observed profiles remain stationary for a 24 h time frame refers to the measurement situation for the calculation of dust radiative effects. To leave no room for misinterpretation we removed this somewhat unnecessary sentence in the revised manuscript: ~~*It is assumed that the observed measurement situation does not change and remains stationary within a 24 h time frame.*~~

14. **Comment: Pxii, L11: 2-5 g/kg, one page before you stated 3-5 g/kg**
We corrected that.

15. **Comment: Fig. 4: DIAL measurements are shown in black not blue**
We made the correction.

16. **Comment: Fig. 4 right: Black and dark blue are difficult to distinguish. Please take a different color.**
You are right. Navy blue and black are difficult to distinguish. We changed the colors to blue and grey in the revised manuscript. In our opinion the profiles in the revised figure are way easier to distinguish.

17. **Comment: Sect. 3.3: According to the text, the radiative effects are calculated for the Saharan dust particles disregarding the water vapor. Is this the case? Please state it clearly**
No this is not the case. Calculations of radiative effects are performed using all information from the conducted lidar measurements including measured water vapor concentrations. We clarified that in the revised manuscript.

18. **Comment: Pxxv, L8-16: This paragraph should be carefully rewritten. 'Calculations of RE_{TOA} show similar results for case (c). (L10)' - Similar to what? In case of negative numbers, what is considered a minimum? (L13-15)**
Thank you for this very valuable comment. We rewrote the whole paragraph and replaced *maxima and minima* as well as *increasing and decreasing* with *strongest and weakest magnitudes* and *strengthening and weakening*. In this way, the paragraph can be much better understood. The changes in the manuscript can be found in the appended marked-up manuscript version.

19. **Comment: Pxxvi, L20: Reference in brackets.**
We removed the brackets.

20. **Comment: Pxxvi, L34: January/February 2020**
You are certainly right. The campaign reached into February. We corrected that.

21. **Comment: Pxxvii, L17: 'and therefore counteracts the development of convection in the MBL'**
We added that.

22. **Comment: Pxxvii, L20: '...were found at intermediate zenith angles for the presented case study' However, case study (c) represents a rather thick SAL and so the reported maximum values should hold for long-range transported dust at Barbados.**
We followed your suggestion and changed the sentence.

23. **Comment: Sometimes your sentences tend to be very long. It would be easier for the reader to split them into two sentences, e.g., Pvii, L21-24 or Pxxv, L21-23**
Following your feedback, we split up several sentences in the revised manuscript. The changes can be found in the marked-up manuscript version.

Reply to Minor Comments of Referee Jeffrey Reid on 19 August 2020

1. **Comment: Page 2 line 1: 'SALs remain relatively undisturbed and can be transported over thousands of kilometers towards the Caribbean or Americas (Carlson and Prospero, 1972; Karyampudi and Carlson, 1988; Karyampudi et al., 1999).'** However, in the PRIDE campaign we showed this is not the case (e.g., Reid et al., 2002, 2003; Maring, 2003) there is considerable variability in dust heights by the time dust reaches the Caribbean. People like the Karyampudi model because it is simple, but it is an idealized situation. Further, the SAL is not always well defined in association with dust transport, especially in January through May. June is a transition month, late July-August is when the Karyampudi SAL model is most appropriate. Indeed, dust transported across the Atlantic in lots of different ways, and the authors language convolutes these mechanisms. During the PRIDE campaign (e.g., Reid et al., 2002), the highest dust concentrations were actually in the marine boundary layer, NOT IN THE SAL. The reasons for this are open to debate (Reid et al. (2003) versus Colarco et al. (2003)).

Thank you for this comment. In the framework of your 'Quick Review' you have already pointed out that the Karyampudi-model is an idealized model which mainly applies to the summer months of transatlantic dust transport. We already made changes to the submitted manuscript as a consequence of the quick reviews and highlighted the variability of transatlantic dust transport in the Discussion. However, in our opinion this issue should already be clarified in the Introduction of the paper. This is why we modified the respective paragraph in the Introduction of the revised manuscript and added the information:

Embedded in the trade wind flow SALs can be transported over thousands of kilometers towards the Caribbean or Americas (Carlson and Prospero, 1972; Karyampudi and Carlson, 1988; Karyampudi et al., 1999). During the summer months from June to August SALs are observed to remain relatively undisturbed during their transatlantic transport. However, previous field campaigns (e.g. the Puerto Rico Dust Experiment PRIDE in 2000), have shown that especially during the winter months dust transport is also occurring at lower atmospheric levels down to sea surface (Reid et al., 2002). Such a transport would modify the aerosol composition inside the boundary layer and would potentially impact the boundary layer state.

2. **Comment: Page 2 Line 13. 'We found enhanced water vapor mixing ratios within the SAL compared to the surrounding dry free troposphere.'** Again, this is true in the context of a well-defined SAL relative to large scale subsidence in the Hadley cell. Under the influence of an easterly wave, there can be quite a lot of moisture around. I have no concern with this study looking at more idealized situations, but it should be mentioned that this analysis is just that, idealized. There is much more variability in the region. I don't expect the authors to handle this full range of complexity, as their point is well made. But they should discuss it.

You are certainly right. To clarify that, we added some sentences in the Discussion and highlighted that water vapor transport is much more complex and may depend on the synoptic situation and the interaction of the SAL with African Easterly waves:

Furthermore, the observed vertical water vapor distribution during NARVAL-II may only be representative for an undisturbed SAL-transport during the summer months. Moisture originating from the outflow of the Inter-tropical convergence zone or from convective systems embedded in African Easterly Waves can modify the vertical moisture distribution in SAL-regions during disturbed transatlantic transports. Questions on the reasons for the variability in the vertical distributions of mineral dust and water vapor as well as whether there is a certain seasonal pattern in these vertical distributions not only at the beginning but also throughout the transatlantic transport can hopefully be answered in near future by analyzing data collected during the recent EUREC⁴A field campaign (Elucidating the Role of Clouds-Circulation Coupling in Climate; Bony et al., 2017) in January/February 2020.

3. **Comment: Page 3, line 11. '... (NARVAL-II) took place in August 2016...' my point exactly. This is a limited time period in the middle of the most representative of Karyampudi.**

Yes you are right. NARVAL-II provided a snapshot of the SAL-situation during the summer months. An analysis of data collected during the SAL-influenced EUREC⁴A campaign will provide valuable insights in the Caribbean dust-situation during subtropical winter. It will be interesting to see how the radiative impacts of transported mineral dust during summer (NARVAL-II) and winter (EUREC⁴A) differ. We added the following

sentence to the Discussion of the revised manuscript: *An analysis of the EUREC⁴A data set will additionally provide valuable insights on the SAL-radiative effects during subtropical winter months.*

4. Comment: Page 5, line 28. I am not sure why you don't make full use of the HSRL here. We know the mass extinction efficiency for dust is around $0.5 \text{ m}^2\text{g}^{-1}$ and you have an extinction measurement. Or if you have noise issues, aerosol backscatter with a mean lidar ratio at least provides linear error propagation (e.g. Reid et al., 2017). Using AERONET retrievals would be a last resort in my mind. In fact, I have my doubts as in mixed environments the retrievals have to apply a mean index of refraction, which does not fit anything.

The calculation of particle mass concentrations using HSRL-extinction measurements together with conversion factors retrieved from the AERONET inversion algorithm is a well known method, which makes full use of the HSRL-capabilities. These factors have even been validated by Groß et al. (2016), who compared in-situ measurements of dust mass concentrations to dust mass concentrations derived from lidar extinction measurements over Barbados. The retrieved mass concentrations from lidar were in good agreement with the concentrations from in-situ measurements. In mixed regimes, we separated the extinction coefficients of mineral dust and marine aerosol, using the method described in Tesche et al. (2009) and Groß et al. (2011). In this way no factors from mixed regimes are applied, but from pure regimes only. We think that this method is the most appropriate method to calculate dust mass concentrations from HSRL-extinction measurements.

5. Comment: Page 7, Line 5. As mentioned in my pre review, I think the Hess models have serious problems with dust, right down to incorrect spectral dependence of extinction and large uncertainties in spectral absorption. I think the authors should look hard at the results of Hansel et al. 2009 and Sokolik and Toon 1998. Again, I don't expect the authors to resolve this, and using OPAC is ok for a baseline study. But the authors should be clear on this point.

We are aware that by using inversion techniques together with OPAC, uncertainties are introduced to the results. However, as you already said, this study represents a baseline study and uncertainties in spectral dependencies of extinction have almost no impact on the presented results.

As already mentioned in the response to your 'Quick Reviews' the well-known OPAC by Hess et al. (1998) has been improved within the framework of the recent update by Koepke et al. (2015) (four years after the publication of Hansell et al., 2011). Within this update the transition from calculations based on Mie theory for spherical mineral dust particles to T-Matrix calculations with assumptions on the aspect ratio distribution of prolate spheroids has been made. This change mainly led to improvements for scattering simulations in the solar range, but could also have implications in the comparison of mass extinction efficiencies discussed in Hansell et al. (2011).

6. Comment: Page 8, line 8 'hygroscopy' should be hygroscopicity.

We corrected that.

7. Comment: Page 9, Figure 2. I am not sure based on these lidar profiles that one can say that the MBL goes to 1.6 km. It really depends on where the cloud tops are on whether or not there is detainment there or if it is a residual layer form somewhere else. Mixed layer is easier to define, but MBL top is a bit amorphous.

Thank you for this comment. Referee #1 already demanded a clear definition of the marine boundary layer (MBL) in this paper. There are many different definitions of the lowermost part of the atmosphere in literature (e.g. Jung et al., 2013; Rittmeister et al., 2017; Groß et al., 2016; Gutleben et al., 2019). As already mentioned in the response to Comment #1 of Referee #1 we follow the MBL-definition made in Gutleben et al. (2019) which seems to be most appropriate for the observations during NARVAL-II: an approximation of the MBL-top is performed by searching for the TWI in dropsonde measurements. It is coming along with a strong hydrolapse and a strong increase of potential temperature.

However, we are aware that in the submitted manuscript a clear statement, that the given MBL and SAL-extents are just approximations from an analysis of dropsonde profiles, is missing so far. We added this information in the text and the figure captions in the revised manuscript. Changes can be found in the marked-up manuscript version.

8. **Comment: Page 10/Page 12 line 10/Page 15 line 30: The authors use potential temperature to define mixing, whereas it really should be equivalent potential temperature. Water vapor profiles for case (b) are well mixed in the middle of the SAL, (c) is distinctly not, with multiple water vapor layers visible corresponding with dust concentration. Mixing ratio should be constant in the presence of mixing. So with the difference in vertical heat shown, why is there stratification? You may want to look at wind shear.**

Thank you for this very valuable comment. We added profiles of equivalent potential temperature (Θ_e) to Figure 4 in the revised manuscript. From surface level to the top of the SALs the profiles of Θ_e mainly follow the shapes of the profiles of r_m . Due to the lack of condensable water vapor in altitudes higher than the SAL-tops, profiles of Θ_e and Θ converge with altitude.

We also performed a dropsonde-analysis for profiles of wind speed and wind shear during RF3 to examine the causes for the observed layering of water vapor inside and below the SAL (not shown in the revised manuscript). Therefore, we interpolated the measurements of the 23 deployed dropsondes in this measurement region along the flight track (Figure 2). It can be seen that the vertical layering of water vapor and particle backscattering inside the SAL is coinciding with vertical changes of wind speed (sharp gradients of wind speed at ~ 3.0 km and ~ 4.5 km altitude). As a result, wind shear is highest at the top of the SAL and at the boundaries of the respective water vapor filaments. In this case, differences in wind shear could be an explanation why vertical mixing processes due to radiative heating are confined to the respective water vapor layers. We added this information to the respective paragraphs in the revised manuscript. Changes can be found in the marked-up manuscript version.

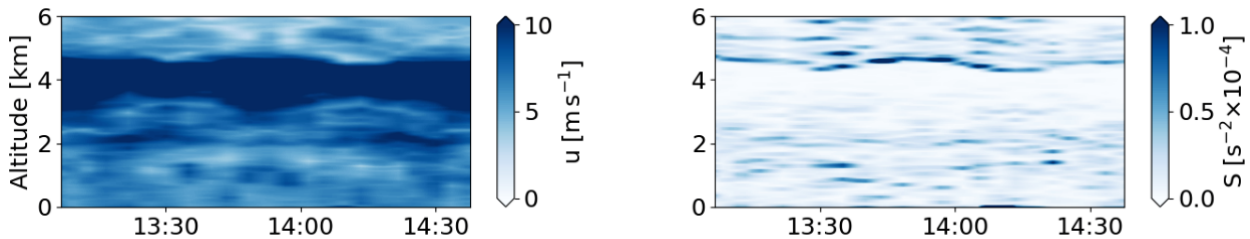


Figure 2: Vertical profiles of wind speed u (right) and wind shear S (left) as measured from dropsondes during RF3 interpolated along the HALO flight path.

References

- Bony, S., and Coauthors, 2017: Eurec4a: a field campaign to elucidate the couplings between clouds, convection and circulation. *Surv. Geophys.*, **38** (6), 1529–1568, doi:10.1007/s10712-017-9428-0.
- Burton, S. P., and Coauthors, 2012: Aerosol classification using airborne high spectral resolution lidar measurements – methodology and examples. *Atmos. Meas. Tech.*, **5** (1), 73–98, doi:10.5194/amt-5-73-2012.
- Carlson, T. N., and J. M. Prospero, 1972: The large-scale movement of Saharan air outbreaks over the northern equatorial Atlantic. *J. Appl. Meteorol.*, **11** (2), 283–297, doi:10.1175/1520-0450(1972)011<0283:TLSMOS>2.0.CO;2.
- Colarco, P. R., O. B. Toon, and B. N. Holben, 2003: Saharan dust transport to the Caribbean during PRIDE: 1. Influence of dust sources and removal mechanisms on the timing and magnitude of downwind aerosol optical depth events from simulations of in situ and remote sensing observations. *J. Geophys. Res.- Atmos.*, **108** (D19), doi:10.1029/2002JD002658.
- Dunion, J. P., and C. S. Velden, 2004: The impact of the Saharan air layer on Atlantic tropical cyclone activity. *B. Am. Meteorol. Soc.*, **85** (3), 353–366, doi:10.1175/BAMS-85-3-353.
- Gamo, M., 1996: Thickness of the dry convection and large-scale subsidence above deserts. *Bound-Lay. Meteorol.*, **79** (3), 265–278, doi:10.1007/BF00119441.

- Groß, S., M. Esselborn, B. Weinzierl, M. Wirth, A. Fix, and A. Petzold, 2013: Aerosol classification by airborne high spectral resolution lidar observations. *Atmos. Chem. Phys.*, **13** (5), 2487–2505, doi:10.5194/acp-13-2487-2013.
- Groß, S., V. Freudenthaler, K. Schepanski, C. Toledano, A. Schäfler, A. Ansmann, and B. Weinzierl, 2015: Optical properties of long-range transported saharan dust over barbados as measured by dual-wavelength depolarization raman lidar measurements. *Atmos. Chem. Phys.*, **15** (19), 11 067–11 080, doi:10.5194/acp-15-11067-2015.
- Groß, S., J. Gasteiger, V. Freudenthaler, T. Müller, D. Sauer, C. Toledano, and A. Ansmann, 2016: Saharan dust contribution to the Caribbean summertime boundary layer – a lidar study during SALTRACE. *Atmos. Chem. Phys.*, **16** (18), 11 535–11 546, doi:10.5194/acp-16-11535-2016.
- Groß, S., M. Tesche, V. Freudenthaler, C. Toledano, M. Wiegner, A. Ansmann, D. Althausen, and M. Seefeldner, 2011: Characterization of saharan dust, marine aerosols and mixtures of biomass-burning aerosols and dust by means of multi-wavelength depolarization and Raman lidar measurements during SAMUM 2. *Tellus B*, **63** (4), 706–724, doi:10.1111/j.1600-0889.2011.00556.x.
- Gutleben, M., S. Groß, and M. Wirth, 2019: Cloud macro-physical properties in Saharan-dust-laden and dust-free North Atlantic trade wind regimes: a lidar case study. *Atmos. Chem. Phys.*, **19** (16), 10 659–10 673, doi:10.5194/acp-19-10659-2019.
- Haarig, M., A. Ansmann, H. Baars, C. Jimenez, I. Veselovskii, R. Engelmann, and D. Althausen, 2018: Depolarization and lidar ratios at 355, 532, and 1064 nm and microphysical properties of aged tropospheric and stratospheric Canadian wildfire smoke. *Atmos. Chem. Phys.*, **18** (16), 11 847–11 861, doi:10.5194/acp-18-11847-2018.
- Haarig, M., A. Ansmann, J. Gasteiger, K. Kandler, D. Althausen, H. Baars, M. Radenz, and D. A. Farrell, 2017a: Dry versus wet marine particle optical properties: RH dependence of depolarization ratio, backscatter, and extinction from multiwavelength lidar measurements during SALTRACE. *Atmos. Chem. Phys.*, **17** (23), 14 199–14 217, doi:10.5194/acp-17-14199-2017.
- Haarig, M., and Coauthors, 2017b: Triple-wavelength depolarization-ratio profiling of Saharan dust over Barbados during SALTRACE in 2013 and 2014. *Atmos. Chem. Phys.*, **17** (17), 10 767–10 794, doi:10.5194/acp-17-10767-2017.
- Hansell, R. A., J. S. Reid, S. C. Tsay, T. L. Roush, and O. V. Kalashnikova, 2011: A sensitivity study on the effects of particle chemistry, asphericity and size on the mass extinction efficiency of mineral dust in the Earth’s atmosphere: from the near to thermal IR. *Atmos. Chem. Phys.*, **11** (4), 1527–1547, doi:10.5194/acp-11-1527-2011.
- Hess, M., P. Koepke, and I. Schult, 1998: Optical properties of aerosols and clouds: the software package OPAC. *B. Am. Meteorol. Soc.*, **79** (5), 831–844, doi:10.1175/1520-0477(1998)079<0831:opoaac>2.0.co;2.
- Jung, E., B. Albrecht, J. M. Prospero, H. H. Jonsson, and S. M. Kreidenweis, 2013: Vertical structure of aerosols, temperature, and moisture associated with an intense African dust event observed over the eastern Caribbean. *J. Geophys. Res.-Atmospheres*, **118** (10), 4623–4643, doi:10.1002/jgrd.50352.
- Karyampudi, V. M., and T. N. Carlson, 1988: Analysis and numerical simulations of the Saharan air layer and its effect on easterly wave disturbances. *J. Atmos. Sci.*, **45** (21), 3102–3136.
- Karyampudi, V. M., and Coauthors, 1999: Validation of the Saharan dust plume conceptual model using lidar, Meteosat, and ECMWF data. *B. Am. Meteorol. Soc.*, **80** (6), 1045–1075, doi:10.1175/1520-0477(1999)080<1045:VOTSDP>2.0.CO;2.
- Koepke, P., J. Gasteiger, and M. Hess, 2015: Technical note: Optical properties of desert aerosol with non-spherical mineral particles: data incorporated to OPAC. *Atmos. Chem. Phys.*, **15** (10), 5947–5956, doi:10.5194/acp-15-5947-2015.
- Mamouri, R.-E., and A. Ansmann, 2016: Potential of polarization lidar to provide profiles of CCN- and INP-relevant aerosol parameters. *Atmos. Chem. Phys.*, **16** (9), 5905–5931, doi:10.5194/acp-16-5905-2016.

- Maring, H., 2003: Vertical distributions of dust and sea-salt aerosols over Puerto Rico during PRIDE measured from a light aircraft. *J. Geophys. Res.*, **108 (D19)**, doi:10.1029/2002jd002544.
- Prospero, J. M., and T. N. Carlson, 1972: Vertical and areal distribution of Saharan dust over the western equatorial North Atlantic Ocean. *J. Geophys. Res.*, **77 (27)**, 5255–5265, doi:10.1029/JC077i027p05255.
- 5 Reid, J. S., and Coauthors, 2002: Dust vertical distribution in the Caribbean during the Puerto Rico Dust Experiment. *Geophys. Res. Lett.*, **29 (7)**, doi:10.1029/2001gl014092.
- Reid, J. S., and Coauthors, 2003: Analysis of measurements of Saharan dust by airborne and ground-based remote sensing methods during the Puerto Rico Dust Experiment (PRIDE). *J. Geophys. Res.- Atmos.*, **108 (D19)**, doi:10.1029/2002jd002493.
- 10 Reid, J. S., and Coauthors, 2017: Ground-based High Spectral Resolution Lidar observation of aerosol vertical distribution in the summertime Southeast United States. *J. Geophys. Res.- Atmos.*, **122 (5)**, 2970–3004, doi:10.1002/2016JD025798.
- Rittmeister, F., A. Ansmann, R. Engelmann, A. Skupin, H. Baars, T. Kanitz, and S. Kinne, 2017: Profiling of Saharan dust from the Caribbean to western Africa – part 1: Layering structures and optical properties from shipborne polarization/Raman lidar observations. *Atmos. Chem. and Phys.*, **17 (21)**, 12 963–12 983, doi:10.5194/acp-17-12963-2017.
- 15 Sokolik, I. N., and O. B. Toon, 1999: Incorporation of mineralogical composition into models of the radiative properties of mineral aerosol from UV to IR wavelengths. *J. Geophys. Res.- Atmos.*, **104 (D8)**, 9423–9444, doi:10.1029/1998JD200048.
- 20 Tesche, M., A. Ansmann, D. Müller, D. Althausen, R. Engelmann, V. Freudenthaler, and S. Groß, 2009: Vertically resolved separation of dust and smoke over cape verde using multiwavelength raman and polarization lidars during saharan mineral dust experiment 2008. *J. Geophys. Res.*, **114 (D13)**, doi:10.1029/2009jd011862.

Radiative effects of long-range-transported Saharan air layers as determined from airborne lidar measurements

Manuel Gutleben¹, Silke Groß¹, Martin Wirth¹, and Bernhard Mayer²

¹Deutsches Zentrum für Luft- und Raumfahrt, Institut für Physik der Atmosphäre, Oberpfaffenhofen, Germany

²Ludwig-Maximilians-University (LMU), Meteorological Institute, Munich, Germany

Correspondence: Manuel Gutleben (manuel.gutleben@dlr.de)

Abstract. The radiative effect of long-range-transported Saharan air layers is investigated on the basis of simultaneous airborne high spectral resolution and differential absorption lidar measurements in the vicinity of Barbados. Within the observed Saharan air layers increased water vapor concentrations compared to the dry trade wind atmosphere are found. The measured profiles of aerosol optical properties and water vapor mixing ratios are used to characterize the atmospheric composition in radiative transfer calculations, to calculate radiative effects of moist Saharan air layers and to determine radiative heating rate profiles. An analysis based on three case studies reveals that the observed enhanced amounts of water vapor within Saharan air layers have a much stronger impact on heating rate calculations than mineral dust aerosol. Maximum mineral dust short-wave heating and long-wave cooling rates are found in altitudes of highest dust concentration (short-wave: $+0.5 \text{ K d}^{-1}$, long-wave: -0.2 K d^{-1} , net: $+0.3 \text{ K d}^{-1}$). However, when considering both aerosol concentrations and measured water vapor mixing ratios in radiative transfer calculations the maximum heating/cooling rates shift to the top of the dust layer (short-wave: $+2.2 \text{ K d}^{-1}$, long-wave: -6.0 to -7.0 K d^{-1} , net: ~~-5.0~~ to -4.0 -5.0 K d^{-1}). Additionally, the net-heating rates decrease with height - indicating a destabilizing effect in the dust layers. Long-wave counter radiation of Saharan air layers is found to reduce cooling at the ~~top~~ tops of the subjacent marine boundary layers and might lead to less convective mixing in these layers. The overall short-wave radiative effect of mineral dust particles in Saharan air layers indicates a maximum magnitude of -40 W m^{-2} at surface level and a maximum of -25 W m^{-2} at the top of the atmosphere.

1 Introduction

Each year during the northern hemispheric summer months from June to August large amounts of Saharan mineral dust particles are transported from the African continent towards the Caribbean islands (Moulin et al., 1997). Dust particles are injected into the atmosphere over the Saharan desert, e.g. by nocturnal low-level jets or convective activity (Schepanski et al., 2009) and form well-mixed convective aerosol layers from ground level to up to 4-6 km height (Esselborn et al., 2008; Ben-Ami et al., 2009; Ansmann et al., 2011). Easterlies subsequently transport the layers westwards over hot desert surfaces towards the Atlantic Ocean. At the Atlantic coast the layers are undercut and lifted by cooler North Atlantic air masses and form elevated layers, the so-called Saharan Air Layers (SALs; Carlson and Prospero, 1972; Prospero and Carlson, 1972).

Embedded in the trade wind flow SALs ~~remain relatively undisturbed and~~ can be transported over thousands of kilometers towards the Caribbean or Americas (Carlson and Prospero, 1972; Karyampudi and Carlson, 1988; Karyampudi et al., 1999). ~~Thus~~ During the summer months from June to August SALs are observed to remain relatively undisturbed during their transatlantic transport. However, previous field campaigns (e.g. the Puerto Rico Dust Experiment PRIDE in 2000), have shown
5 that especially during the winter months dust transport is also occurring at lower atmospheric levels down to sea surface (Reid et al., 2002). Such a transport would modify the aerosol composition inside the boundary layer and would potentially impact the boundary layer state.

Either way, Saharan mineral dust aerosol layers cannot be understood as a local phenomena close to their source regions. They have an impact on the radiation budget as well as on the formation and physical properties of clouds over large areas far
10 away from their origin.

Optical and microphysical properties of long-range-transported Saharan mineral dust (~~Groß et al., 2015; ?; Toledano et al., 2019~~)
(Groß et al., 2015; Haarig et al., 2017a; Toledano et al., 2019) were investigated during the SALTRACE field campaign (Saha-
ran Aerosol Long-range Transport and Aerosol-Cloud-Interaction Experiment; Weinzierl et al., 2017). Studies that aimed to
quantify the radiative effects of SALs concentrated on regions near Africa at the beginning of transatlantic transport (Li et al.,
15 2004; Zhu et al., 2007; Kanitz et al., 2013). However, detailed studies regarding radiative effects of long-range-transported
SALs are missing.

Gutleben et al. (2019a) investigated a SAL upstream the Caribbean island of Barbados using combined High Spectral
Resolution Lidar (HSRL) and water vapor Differential Absorption Lidar (DIAL) technique. ~~We~~ They found enhanced water
vapor mixing ratios within the SAL compared to the surrounding dry free troposphere. From radio-soundings close to the
20 source region ~~we~~ they inferred an enhancement of water vapor within the SAL already at the beginning of its long-range
transport. Radiosonde measurements and Raman lidar measurements conducted by Jung et al. (2013) and Kanitz et al. (2014)
support these findings. They both show enhanced water vapor concentrations as high as 5 g kg^{-1} within SALs.

Water vapor represents the Earth's strongest greenhouse gas and model calculations indicate that especially after long-range
transport SAL-heating rates are highly sensitive to the used water vapor profile (Wong et al., 2009). However, previous studies
25 which focused on the radiative effect of SALs close to their source regions lacked simultaneous measurements of water vapor
and aerosol optical properties and had to assume the water vapor vertical distribution from standard atmospheres or model
simulations. ~~Gutleben et al. (2019)~~ Gutleben et al. (2019a) however, showed that radiative heating caused by SAL-water vapor
has a much greater magnitude than radiative heating by SAL-mineral dust particles and might alter the radiative heating rate
profile from the bottom to the top of the SAL. Moreover, SAL-water vapor is not only influencing the SAL-thermodynamic
30 structure itself but potentially has an impact on surrounding atmospheric layers.

Differences in shallow marine cloudiness between dust-free and dust-laden North Atlantic trade wind regions were found
by Gutleben et al. (2019b), with the dust-laden regions containing less, shallower and smaller clouds. ~~We~~ They conjectured
that differences in radiative transfer could cause the observed changes. A suppressing characteristic of SAL on convection
was also found by Wong and Dessler (2005), who showed that the convection barrier increases with increasing aerosol optical

depth of the SAL. However, up to now it is still not understood how changes in radiative transfer could modify shallow marine cloudiness in dust-laden trade wind regions.

The aim of this study is to investigate the radiative effect of long-range-transported SALs and to study their impact on the subjacent boundary layer. For this purpose, simultaneous measurements of water vapor concentrations and aerosol optical properties by an airborne lidar system during the Next-generation Aircraft Remote-Sensing for Validation Studies-II (NARVAL-II; Stevens et al., 2019) in August 2016 are used. [The measurements are utilized](#) to characterize the vertical structure of both aerosols and water vapor mixing ratio from flight level down to the surface. The retrieved lidar profiles are utilized for the calculation of radiative heating rate profiles of both aerosols and water vapor using the radiative transfer model libRadtran (Library Radiative Transfer; Mayer and Kylling, 2005; Emde et al., 2016). Moreover, the radiative effect of long-range-transported SALs at surface level as well as at the top of the atmosphere (TOA) is investigated.

This paper is structured as follows. In Section 2 an overview of the NARVAL-II campaign, the applied instruments and the used radiative transfer model setup is given. Section 3 shows the results of radiative transfer calculations for three representative case studies during NARVAL-II with different vertical dust layer extents and optical thicknesses. Results are discussed in Section 4 and focus on the radiative impact of long-range-transported SALs on the subjacent marine boundary layer (MBL) and atmospheric stability. Section 5 concludes this paper and gives a short summary.

2 Methods

2.1 The NARVAL-II field campaign

The Next-generation Aircraft Remote-Sensing for Validation Studies-II (NARVAL-II) took place in August 2016 and aimed at studying the subtropical North Atlantic atmospheric circulation using a combination of airborne remote sensing instruments (Stevens et al., 2019). Grantley Adams International Airport on Barbados (TBPB, 13° 04' 29" N, 59° 29' 33" W) served as air base for 10 measurement flights over the subtropical North Atlantic Ocean with the German High Altitude and Long range research aircraft HALO (Krautstrunk and Giez, 2012). During the campaign the aircraft was equipped with the lidar system WALES (Wirth et al., 2009) and a set of active and passive remote sensing instruments, i.e. the HALO Microwave Package HAMP (Mech et al., 2014; Ewald et al., 2019), the hyper spectral cloud and sky imager specMACS (Ewald et al., 2016) and the Spectral Modular Airborne Radiation measurement System SMART (Wendisch et al., 2001). In addition, a total number of 218 dropsondes were launched during the flights for measurements of the atmospheres thermodynamic state.

2.2 The WALES instrument

WALES is an airborne lidar system which was developed at the Institute for Atmospheric Physics of the German Aerospace Center (Wirth et al., 2009). The system is designed as a Differential Absorption Lidar (DIAL) for measurements of atmospheric water vapor distributions and operates at four different wavelengths around the water vapor absorption bands at 935 nm. In addition to the DIAL capabilities, WALES is equipped with a polarization sensitive High Spectral Resolution Lidar (HSRL)

Table 1. Vertical resolution of the radiative transfer model.

Altitude [km]	Resolution [km]
0.0 to 10.0	0.1
10.0 to 30.0	1.0
30.0 to 60.0	10.0
60.0 to 120.0	20.0

channel at 532 nm for cloud and aerosol characterization (Esselborn et al., 2008). As a result, WALES is able to perform simultaneous measurements of particle extinction coefficients ($\alpha_{p(532)}$), backscatter ratios ($R_{532} = 1 + \beta_{p(532)}/\beta_{m(532)}$ - with $\beta_{p(532)}$ and $\beta_{m(532)}$ being the the particle and molecular backscatter coefficients) and particle linear depolarization ratios ($\delta_{p(532)}$) at 532 nm as well as water vapor mass mixing ratios (r_m) from flight altitude to surface level. DIAL and HSRL measurements are temporally averaged for noise reduction. As a result horizontal resolutions are of approximately 0.2 km for HSRL measurements and 3.0 km for DIAL measurements at typical aircraft speeds around 200 ms^{-1} . WALES measures in near nadir direction ($2^\circ - 3^\circ$ off-nadir angle) with vertical resolutions of 15 m. Pulse repetition rates of 10 ms between online and offline pulses allow high quality water vapor measurements with relative uncertainties of less than 5 % (Kiemle et al., 2008). Relative uncertainties of backscatter, particle linear depolarization and extinction measurements sum up to 5 %, 10-16 %, and 10-20 %, respectively (Esselborn et al., 2008).

2.3 The radiative transfer model libRadtran

Calculations of both downward and upward irradiances as well as atmospheric heating rates are performed utilizing the radiative transfer equation solver DISORT (Stamnes et al., 1988) with an improved intensity correction (Buras et al., 2011). The solver is embedded in the Library Radiative Transfer model (libRadtran; Mayer and Kylling, 2005; Emde et al., 2016) and is applied with 16 streams in the short-wave ($0.12-4.0 \mu\text{m}$) and long-wave ($2.5-100.0 \mu\text{m}$) spectra. At lower tropospheric levels (0-10 km) the model grid is set to vertical resolutions of 0.1 km. To save computational time the grid setting is changed to coarser resolutions at higher altitudes (see Table 1).

Time-expensive line-by-line calculations of spectral molecular absorption in the short-wave and long-wave spectral ranges are avoided by employing the sufficiently accurate correlated k-distribution absorption band parametrizations (Kato et al., 1999; Fu and Liou, 1992). Irradiances are then calculated by integrating over the respective parametrized absorption bands and height resolved diurnally averaged heating rates in the short-wave and long-wave spectra are derived from the difference in calculated radiation flux at the particular height intervals solving,

$$\frac{\delta T}{\delta t} = - \frac{1}{c_p \rho(z)} \frac{\delta F_{\text{net}}}{\delta z}(z) \frac{\delta T}{\delta t}(z) = - \frac{1}{c_p \rho(z)} \frac{\delta F_{\text{net}}}{\delta z}(z) \quad (1)$$

at any vertical level z . Here, $\frac{\delta T}{\delta t}(z)$ is the change in temperature with time at altitude z , c_p is the specific heat capacity of air at constant pressure, $\rho(z)$ is the altitude dependent air density and $\frac{\delta F_{\text{net}}}{\delta z}(z)$ represents the vertical change in

net radiative flux at altitude z . The model temperature is parametrized using colocated dropsonde measurements. Reference profiles described by Anderson et al. (1986) are used to parametrize the trace gas concentrations from 0-120 km altitude. However, water vapor profiles and any information on the atmospheric aerosol composition underneath the aircraft are taken from WALES lidar measurements which are interpolated accordingly to fit the model grid.

- 5 To minimize uncertainties in surface albedo (Claquin et al., 1998; Liao and Seinfeld, 1998) the bidirectional reflectance distribution function (BRDF; Cox and Munk, 1954a, b; Bellouin et al., 2004) is used. The BRDF derives sea surface albedo from 10 m-wind speeds measured by dropsondes and sea swell. Based on measurements by the MODIS-Aqua/Terra satellite during the field campaign, sea surface temperature is set to a fixed value of 302 K.

2.4 Aerosol optical properties from lidar measurements

- 10 In this study, the characterization of aerosol and water vapor profiles in libRadtran is performed using WALES DIAL and depolarization lidar measurements. Therefore, a method to identify profile-regions of different aerosol species and aerosol concentrations using lidar measurements of $\alpha_{p(532)}$, R_{532} , $\delta_{p(532)}$ and r_m was developed and is discussed in the following.

2.4.1 Aerosol classification

- 15 WALES lidar profiles of ~~partitee~~-particle linear depolarization ratio $\delta_{p(532)}$ can be used to detect and identify Saharan dust marine aerosols in vertical atmospheric columns (Burton et al., 2012; Groß et al., 2013). $\delta_{p(532)}$ for Saharan dust near source regions fluctuates around 0.3 (Freudenthaler et al., 2009; Tesche et al., 2009b; Groß et al., 2011b) ~~and recent studies~~. Groß et al. (2015) showed that this ratio remains unchanged after long-range transport across the subtropical North Atlantic Ocean (~~Burton et al., 2012; Groß et al., 2015~~). Marine aerosol is composed of sea salt and water-soluble parts and is weakly depolarizing in a moist environment. Dry and stronger depolarizing marine aerosol ($\delta_{p(532)} > 0.04$; ~~Murayama et al., 1999; Sakai et al., 2010~~) Murayama et al., 1999; Sakai et al., 2010; Haarrig et al., 2017b) is therefore not expected since relative humidity ~~inside the MBL at lowest atmospheric levels~~ was found to be always greater than 80%. Other aerosol types, like e.g. African biomass burning aerosols, are also not expected in the measurement region and no evidence for such types was found across the subtropical North Atlantic Ocean by looking at satellite imagery. As a result, $\delta_{p(532)}$ is a good proxy for the differentiation of mineral dust and less depolarizing marine aerosol (Sakai et al., 2010; Burton et al., 2012; Groß et al., 2013) in NARVAL-II
- 25 WALES lidar profiles. In this way three aerosol regimes can be determined in the dataset:

I. pure mineral dust regime: $\delta_{p(532)} \geq 0.26$,

II. pure marine aerosol regime: $\delta_{p(532)} \leq 0.04$,

III. mixed regime - marine aerosol mixed with mineral dust: $0.04 < \delta_{p(532)} < 0.26$.

- Clear and aerosol-free regions are detected via filtering for no evident particle-backscattering ($R_{532} < 1.2$). Cross sections of an aerosol mask along the HALO flight tracks for libRadtran aerosol input are generated using these criteria.
- 30

In addition to the application of the detection scheme, the Saharan origin of detected mineral dust layers is verified utilizing the HYbrid Single Particle Lagrangian Integrated Trajectory model (HYSPLIT; Stein et al., 2015) with NCEP GDAS (National Centers for Environmental Prediction Global Data Assimilation System) input data (shown in Gutleben et al., 2019b). Starting locations and times for the backward trajectory calculations were chosen to match the center of detected mineral dust layers in lidar data.

2.4.2 Conversion of aerosol extinction coefficients to aerosol mass concentrations

To run UVSPEM with aerosol input, particle mass concentrations in the classified aerosol regimes have to be determined.

According to Groß et al. (2016), conversion factors can be used to convert measured $\alpha_{p(532)}$ to mineral dust and marine aerosol concentrations per unit volume ($c_{v,dust}$, $c_{v,marine}$). These factors are taken from results of the AERONET inversion algorithm by Mamouri and Ansmann (2016) which derived a factor $\nu_{dust(532)} = c_{v,dust}/\alpha_{p(532),dust} = 6.5 \pm 1.8 \times 10^{-7} \text{ m}$ for presented by Mamouri and Ansmann (2016) and are given in Groß et al. (2016). For long-range-transported Saharan dust a conversion factor of $\nu_{dust(532)} = c_{v,dust}/\alpha_{p(532),dust} = 0.65 \times 10^{-6} \text{ m}$ was derived. Due to the similar size distribution of mineral dust and marine aerosols, the AERONET inversion deduced a similar conversion factor of $\nu_{marine(532)} = c_{v,marine}/\alpha_{p(532),marine} = 7.2 \pm 3.7 \times 10^{-7} \text{ m}$ $\nu_{marine(532)} = c_{v,marine}/\alpha_{p(532),marine} = 0.66 \times 10^{-6} \text{ m}$ for marine aerosol. These values are adopted for this study. Mineral dust and marine aerosol mass concentrations ($c_{m,dust}$, $c_{m,marine}$) are then calculated by multiplying the derived aerosol volume concentrations with typical particle densities of $\rho_{dust} = 2.5 \text{ g cm}^{-3}$ for long-range-transported mineral dust and $\rho_{marine} = 2.2 \text{ g cm}^{-3}$ for marine aerosol. Those particle densities are based on a study by Kaaden et al. (2009) who showed that SALs consist of a mixture of mineral dust particles together with sulfate particles.

The above equations allow the characterization of aerosol mass concentrations in the pure mineral dust regime (I) and marine aerosol regime (II). However, in mixed regimes (III) which appear frequently over the North Atlantic Ocean when SAL-mineral dust is settling to lower atmospheric levels, the mineral dust contribution to $\alpha_{p(532)}$ of the total aerosol mixture has to be determined before the application of the conversion coefficients. The aerosol extinction coefficient at 532 nm of a marine-mineral dust aerosol mixture $\alpha_{p(532),mix}$ can be written as,

$$\begin{aligned} \alpha_{p(532),mix} &= \alpha_{p(532),dust} + \alpha_{p(532),marine} \\ &= (1 - x) \alpha_{p(532),mix} + x \alpha_{p(532),mix}, \end{aligned} \quad (2)$$

with $\alpha_{p(532),marine}$ and $\alpha_{p(532),dust}$ being the marine aerosol and mineral dust particle extinction coefficient at 532 nm and $x = \alpha_{p(532),dust}/\alpha_{p(532),mix}$.

Using the known lidar ratios of marine and mineral dust aerosol at 532 nm ($S_{p(532),marine} \simeq 18$ and $S_{p(532),dust} \simeq 47$; Burton et al., 2012; Groß et al., 2013) and following the methods described in Tesche et al. (2009a) and Groß et al. (2011a) one can calculate the fraction x of dust contributing to the total particle extinction coefficient of the mixture,

$$x = \frac{D_{marine}}{D_{marine} + D_{dust}} \quad x = \frac{D_{marine}}{D_{marine} + D_{dust}} \quad (3)$$

Table 2. OPAC particle type composition of lidar derived aerosol regimes used in the radiative transfer simulations. [Shown percentages refer to mass mixing ratios.](#)

Regime	OPAC component	Mix. ratio
marine aerosol	sea salt (acc. mode)	92.8 %
	water-soluble	5.8 %
	sea salt (coarse mode)	1.4 %
mineral dust	mineral (acc. mode)	74.7 %
	mineral (coarse mode)	20.2 %
	mineral (nuc. mode)	3.3 %
	water-soluble	1.8 %

with the coefficients D_{dust} and D_{marine} : D_{dust} and D_{marine} :

$$D_{dust} := \frac{\delta_{p(532),dust} - \delta_{p(532),mix}}{S_{p(532),dust}(1 + \delta_{p(532),dust})} \quad D_{dust} := \frac{\delta_{p(532),dust} - \delta_{p(532),mix}}{S_{p(532),dust}(1 + \delta_{p(532),dust})} \quad (4)$$

$$D_{marine} := \frac{\delta_{p(532),mix} - \delta_{p(532),marine}}{S_{p(532),marine}(1 + \delta_{p(532),marine})} \quad D_{marine} := \frac{\delta_{p(532),mix} - \delta_{p(532),marine}}{S_{p(532),marine}(1 + \delta_{p(532),marine})} \quad (5)$$

- 5 Finally, Eq. (3), $\nu_{dust(532)}$ and $\nu_{marine(532)}$ as well as ρ_{dust} and ρ_{marine} are used to calculate mineral dust and marine aerosol particle mass concentrations in mixed aerosol regimes (III).

2.4.3 OPAC aerosol micro-physical properties

In a last step, converted aerosol mass concentrations are related to aerosol optical properties that are needed for radiative transfer calculations, i.e. the phase function $P(\Theta)$ and the single scattering albedo ω . Those properties are commonly modeled using size distributions and spectral refractive indices of the desired aerosol species. Model-assumptions always represent some source of uncertainty. For example, Yi et al. (2011) showed that different representations of particle shapes result in a change of $P(\Theta)$ and can cause up to 30 % difference in the dust radiative forcing at top of the atmosphere (TOA). To minimize errors resulting from wavelength-interpolations Hess et al. (1998) established the readily available spectrally resolved OPAC database (Optical properties of Aerosols and Clouds) ~~which~~. It includes modeled information on the above mentioned aerosol optical properties for 61 wavelengths in the spectral range from 0.25-40 μm for various aerosol species. OPAC is a widely used data base in aerosol models and retrievals (e.g. Kim et al., 2004; Liu et al., 2004; Patadia et al., 2009) as well as general circulation and climate models for calculations in both the short-wave and the long-wave spectra. Thus, it is an appropriate tool to link lidar derived aerosol mass concentrations to aerosol optical properties in the classified aerosol regimes.

OPAC sea salt and water-soluble particle microphysical properties are modeled under the assumption of spherical particles using Mie-Theory (Mie, 1908). The assumption of spherical particles is legitimate for radiative transfer simulations in the

period of NARVAL-II since no dry and aspherical marine aerosol particles are expected at observed relative humidities of greater 80 % inside the derived marine aerosol regimes (Murayama et al., 1999; Sakai et al., 2010). Thus, a humidity dependent marine aerosol composition which refers to WALES measurements of water vapor mixing ratios together with dropsonde-derived temperature profiles is used in this study (see Table 2).

5 Mineral dust particles however, are characterized by highly irregular shapes (Falkovich et al., 2001; Kandler et al., 2011). Hence, an assumption of spherical mineral dust particles in radiative transfer models using Mie-Theory is inappropriate and may lead to wrong results. Especially if particles are significantly larger than the transmitted wavelength (which is the case for most backscatter lidar systems) phase functions of aspherical particles are characterized by an increased amount of side-ward but a reduced amount of backward scattering compared to spherical particles (Koepke and Hess, 1988; Gobbi et al., 10 2002; Nousiainen, 2009; Wiegner et al., 2009; Gasteiger et al., 2011; Sakai et al., 2014). For this reason mineral dust particle micro-physical properties were updated in the latest OPAC version (v4.0; Gasteiger et al., 2011; Koepke et al., 2015) ~~and~~. They are now calculated by means of the T-matrix method (Waterman, 1971) under assumptions of an aspect ratio distribution for prolate spheroids observed during the Saharan mineral dust experiments SAMUM-I and SAMUM-II (Kandler et al., 2009, 2011). Several studies have shown that T-matrix theory substantially improves the agreement between measured and modeled 15 aerosol optical properties of aspherical mineral dust particles (Mishchenko et al., 1997; Kahnert et al., 2005; Gasteiger et al., 2011) and are thus motivating its use in this study.

Results obtained from measurements during SALTRACE (Weinzierl et al., 2017) showed that the size distribution of long-range-transported mineral dust does not change significantly compared to the distributions measured at source regions. Gravitational settling processes of large sub-micron particles in the course of the SAL-transatlantic transport are of a smaller mag- 20 nitude than expected from Stokes gravitational settling calculations. Moreover, Denjean et al. (2015) found that the chemical composition and ~~hygroscopy~~ hygroscopicity of mineral dust remains unchanged after long-range transport. Thus, a mixture proposed by Hess et al. (1998) which consists of four OPAC v4.0-components for desert aerosol optical properties is assumed in this paper (see Table 2).

25

3 Results

3.1 NARVAL-II lidar measurements

During two NARVAL-II-research flights on 12 and 19 August 2016 pronounced elevated SALs could be observed. On 12 August (takeoff: 11:43 UTC; landing: 19:37 UTC) dust layers covered the whole research area. This is also seen in MODIS 30 (Moderate Resolution Imaging Spectroradiometer) total column Aerosol Optical Depth (AOD) which took values around 0.3 along the whole flight track (Figure 1). In contrast, the research flight on 19 August (takeoff: 12:28 UTC; landing: 20:52 UTC)

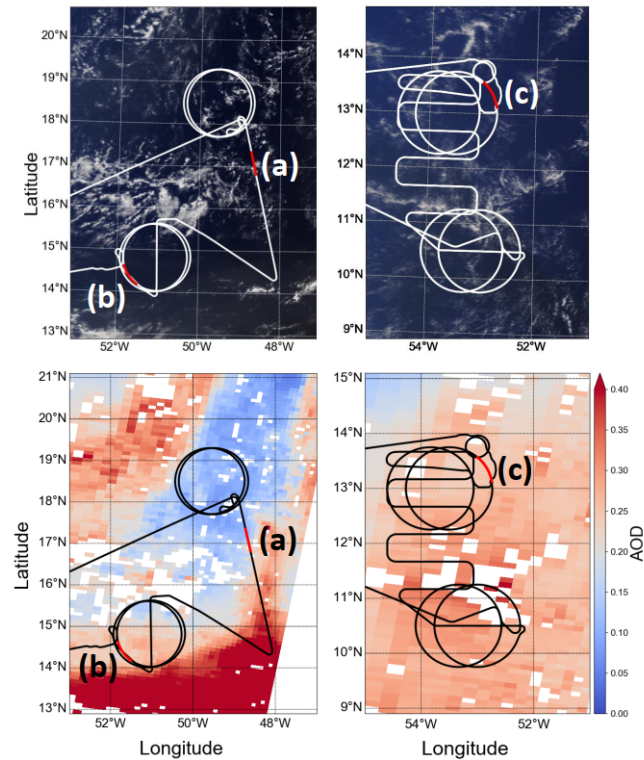


Figure 1. Flight tracks of the research flights conducted on 12 (right) and 19 (left) August 2016 on top of images showing MODIS (MODerate-resolution Imaging Spectroradiometer) true color (top) and Aerosol Optical Depth (AOD, bottom) around 13:40 UTC. Red lines and labels indicate the discussed flight segments (cases (a), (b) and (c)).

led over trade wind regions comprising elevated mineral dust layers ($AOD > 0.3$) as well as regions free of mineral dust and is therefore suitable for a comparison of radiative effects in SAL-influenced regions and SAL-free regions.

In this study three representative cloudless 5 min-lidar cross sections observed during these two research flights are used for radiative transfer calculations (Figures 2). MODIS imagery of the respective regions is additionally used to ensure that that
5 no cirrus clouds have been present above the observed lidar scenes. While the first case represents a SAL-free scenario with some residual mineral dust at low atmospheric levels, the other two cases are both characterized by a long-range-transported SAL. Measured vertical profiles of both R_{532} and $\delta_{p(532)}$ are used for the detection of the SAL-outlines. From enhanced values of R_{532} and typical values of $\delta_{p(532)}$ for mineral dust the vertical extent of SALs can be determined. Additionally, an
10 approximation of the extent of the lowest layer in a marine atmosphere - the marine boundary layer (MBL) - can be determined.
The MBL represents a well mixed layer that is characterized by high humidity. As the MBL is confined by the TWI, its upper limit is coming along with a strong increase of potential temperature and a pronounced hydrolapse (Gutleben et al., 2019b).

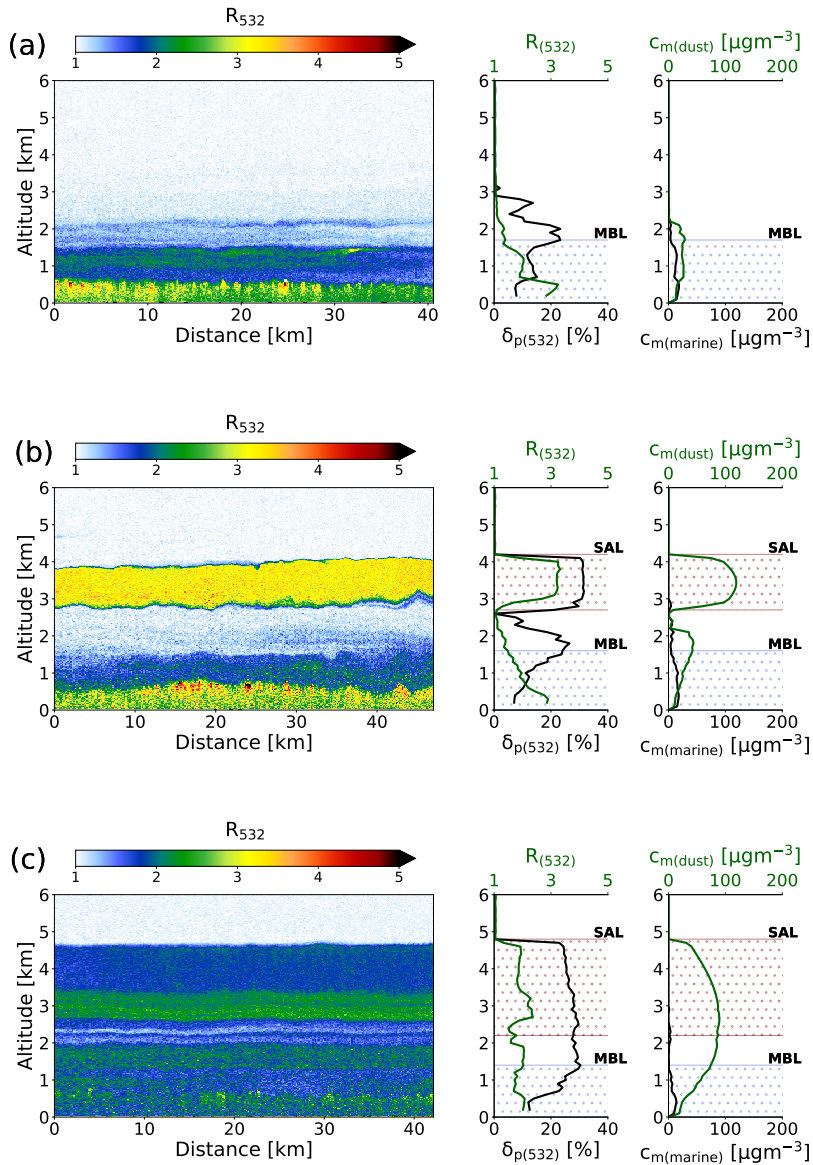


Figure 2. Left: cross-sections of WALES backscatter ratio $R_{(532)}$; Middle: averaged profiles of particle linear depolarization ratios $\delta_p(532)$ (black) and backscatter ratio $R_{(532)}$ (green); Right: derived aerosol mass concentrations ($C_m(\text{dust})$ (redgreen) and $C_m(\text{marine})$ (blueblack)) for case (a) and (b) on 19 Aug 2016 as well as case (c) on 12 Aug 2016.

By searching for those features in measured profiles of r_m (DIAL) and Θ (dro sondes), an approximation of the vertical extent of the MBL is additionally outlined.

All the three selected cross sections are of approximately 50 km length and described in the following:

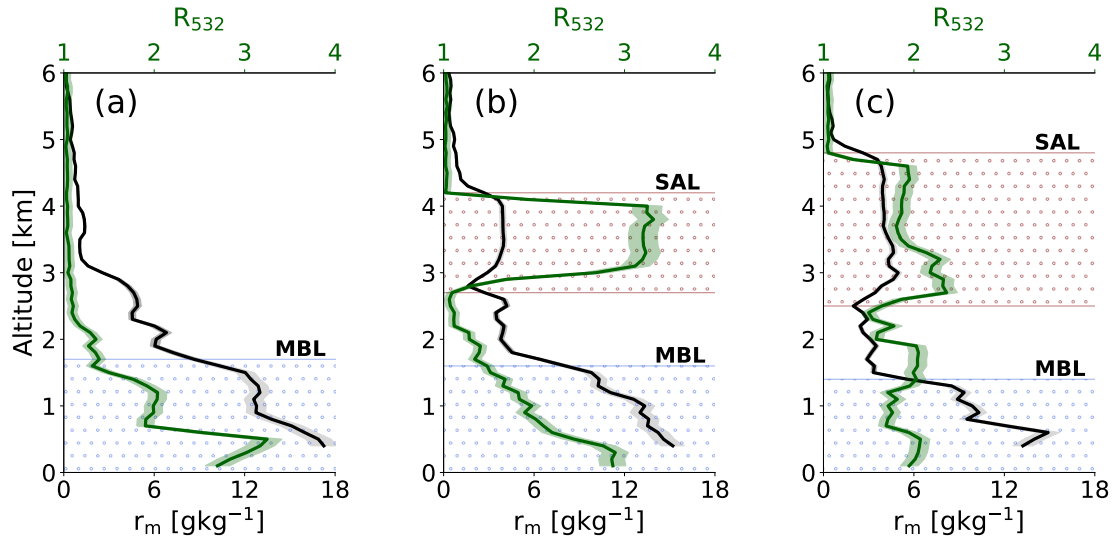


Figure 3. Averaged vertical profiles of backscatter ratio (R_{532}) and water vapor mass mixing ratio (r_m) for cases (a),(b) and (c). Shaded: estimated measurement uncertainties. Colored height intervals highlight the approximate ranges of the Saharan air layer (SAL; orange/dotted) and marine boundary layer (MBL; light-green/light-blue/dotted).

(a) *SAL-free case - 19 Aug 2016 (16:51-16:56 UTC):*

This case represents a SAL-free measurement segment during NARVAL-II. Lidar profiles of R_{532} and $\delta_{p(532)}$ show no dust-signatures in altitudes greater 3 km. In the MBL both marine and mineral dust aerosol particles coexist (settling dust particles) and a maximum aerosol extinction coefficient of 0.03 km^{-1} was measured inside the MBL. $\delta_{p(532)}$ ranges from roughly 0.05-0.25 and aerosol mass concentrations of both marine and mineral dust aerosol reach maximum values of approximately $30 \mu\text{g m}^{-3}$. Above the MBL some signatures of depolarizing particles ($\delta_{p(532)} < 0.25$) with weak backscatter can be identified. Those signatures are most likely caused by settling dust particles from the dissipating SAL nearby (see Figure 1).

(b) *Elevated SAL - 19 Aug 2016 (14:26 - 14:31 UTC):*

The second case represents a scenario with a detected elevated and long-range-transported SAL extending from 3-4 km altitude. The SAL shows increased backscatter ratios around 3.5 and high particle linear depolarization ratios > 0.26 . $\delta_{p(532)}$ and $R_{(532)}$ profiles feature sharp gradients to the above free-troposphere and to lower atmospheric levels. The SAL itself is associated with evenly distributed mineral dust mass concentrations of approximately $120 \mu\text{g m}^{-3}$ and aerosol extinction coefficients around 0.07 km^{-1} . Marine aerosols are mainly confined to the MBL which extends from about 0.0-1.6 km altitude. Similar to case (a) the aerosol composition within the MBL is not exclusively characterized

by marine aerosols but also contains portions of mineral dust aerosols. An intermediate layer showing small values of $\delta_{p(532)}$, $c_{m(\text{dust})}$ and $R_{(532)}$ is located in-between the MBL and the SAL and ranges from about 1.6-2.8 km altitude.

(c) *Thick SAL - 12 Aug 2016 (14:26 - 14:31 UTC):*

5 The third scenario represents the geometrically thickest SAL that has been observed during the whole NARVAL-II campaign. Measured $\delta_{p(532)}$ around 0.3 clearly indicate the presence of Saharan mineral dust from ground level to almost 5 km altitude. The $R_{(532)}$ -profile also shows enhanced particle backscatter greater 2.0 in these altitudes. Compared to case (b) the observed SAL in case (c) shows some vertical layering in backscatter ratio. As it coincides with vertical changes of wind speed (sharp gradients of wind speed at ~ 3.0 km and ~ 4.5 km altitude, not shown), wind shear may be the reason for the layering. Profiles of aerosol mass concentration highlight a pure dust regime ($c_{m(\text{dust})} \approx 100 \mu\text{g m}^{-3}$;
10 aerosol extinction coefficients around 0.06 km^{-1}) at altitudes ranging from approximately about 1.5-5.0 km altitude transitioning to a mixed marine and dust aerosol regime at lower atmospheric levels (about 0-1.5 km). The lidar measurements again do not indicate a pure marine aerosol regime at low altitudes. Both marine and settling mineral dust aerosol is found in the MBL (~~0-1.5~~about 0 to 1.5 km).

All observed SALs during the NARVAL-II period were associated with enhanced concentrations of water vapor compared to
15 the surrounding dry free trade-wind environment (Gutleben et al., 2019a). r_m and $R_{(532)}$ in the lidar profiles (b) and (c) also show a distinct correlation (Figure 3). The SALs show almost uniformly increased water vapor mixing ratios ranging from 3-5 g kg^{-1} compared to the surrounding free-troposphere ~~-(case (b): 2.8-4.2 km km altitude; case (c): 2.5-4.8 km).~~ ~~Case (a) however, indicates that no distinct correlation of enhanced km altitude).~~ Measured profiles of r_m and $R_{(532)}$ for case (a) show that no enhanced water vapor concentrations could be observed in ~~a~~the SAL-free troposphere. The water vapor profile
20 shows a drop of r_m to values smaller 1 g kg^{-1} at altitudes greater 3 km, indicating the transition from the MBL to the dry free troposphere. Such a drop in humidity (which is coming along with a strong trade wind inversion caused by Heady cell subsidence) was observed during most SAL-free periods in NARVAL-II, and is discussed by Gutleben et al. (2019b) in the framework of a detailed dropsonde analysis.

Enhanced water vapor concentrations in SAL-altitudes are already seen at the beginning of the transport (using HYSPLIT
25 backward trajectories), when analyzing radiosonde profiles from operationally launched sondes at Dakar/Senegal four days before the measurements on 8 Aug 2016 and 15 Aug 2016 (Gutleben et al., 2019a).

3.2 Saharan ~~Air Layer Heating~~ air layer heating rates

Profiles of calculated short-wave, long-wave and net heating rates (24 h-averaged) for the three selected case studies are shown in Figure 4. Since WALES is able to measure both water vapor mixing ratios and aerosol optical properties, total heating rate
30 profiles and contributions of mineral dust to total heating rate profiles can be derived. The dust-contribution to the total heating rate is derived as the difference between heating rates that consider dust in the model and heating rates with no dust in the model atmosphere.

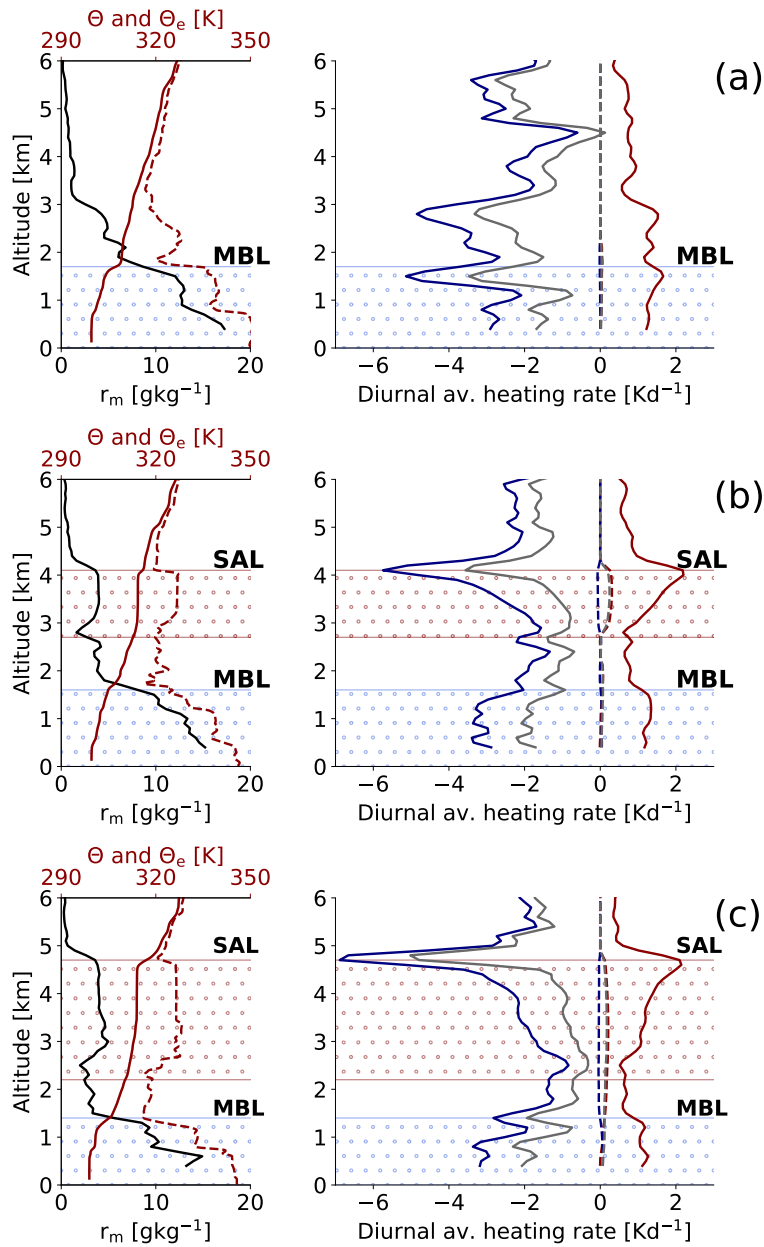


Figure 4. Left: the vertical profiles of derived water vapor mass mixing ratio from DIAL measurements (black), potential temperature Θ (red-solid) and equivalent potential temperature Θ_e (red-dashed) from dropsonde measurements (red) for the three scenarios. Right: the diurnally averaged net (black), short-wave (red) and long-wave (blue) heating rates (solid). Dashed lines illustrate the aerosol-contributions to the total heating rate profiles. Colored height intervals highlight the approximate extent of observed Saharan air layers (SAL; red-dotted) and marine boundary layers (MBL; blue-dotted).

Observed SALs in case (b) and (c) are ~~well-mixed (constant potential temperature characterized by constant potential temperatures~~ Θ around 315 K) and show enhanced water vapor mass mixing ratios in the range from ~~2-5~~ 3-5 g kg^{-1} compared to the surrounding dry free atmosphere. ~~This is also reflected in increased equivalent potential temperatures Θ_e of approximately 330 K inside the SALs.~~ Both profiles have strong gradients of r_m and Θ and Θ_e at the upper edge of the SAL (at the boundary to the above dry and aerosol-free trade wind atmosphere) indicating the two well-known SAL-related bounding inversions (Lilly, 1968). The MBL in all three cases is characterized by high relative humidities (r_m : 10-16 g kg^{-1}) and is capped by a temperature inversion (trade wind inversion) and a pronounced hydrolapse (r_m drops from >15 to approximately 5 g kg^{-1}).

Calculated profiles of diurnally averaged mineral dust short-wave heating rates for mean profiles of case (b) and (c) indicate an atmospheric heating of less than 0.5 K d^{-1} in SAL-altitudes. Maximum short-wave heating is hereby found in altitudes of highest dust mass concentration (case (b): ~ 3.5 km; case (c): 2.5 km). Also long-wave cooling rates of dust are strongest at altitudes of highest dust mass concentration ($\sim 0.2 \text{ K d}^{-1}$). This results in a small net warming effect of long-range-transported dust aerosols of approximately 0.3 K d^{-1} for both cases (b) and (c). The net mineral dust radiative heating rate for the SAL-free case (a) is limited to the lowest atmospheric levels and takes small values of less than 0.1 K d^{-1} .

Due to water vapor absorption and emission the total heating and cooling rate profiles have a completely different shape. Largest water vapor absorption of solar radiation takes place at the uppermost levels of the SAL leading to strong heating at these levels. Long-wave cooling due to emission of radiation towards space is also strongest at the top edge of the SAL since there is no heating from atmospheric counter radiation from higher atmospheric levels. This is why greatest total heating and cooling rates are found at the upper edge of both observed SALs (short-wave: $\sim 2.2 \text{ K d}^{-1}$ (both cases); long-wave: -6 K d^{-1} (case (b)) and -7 K d^{-1} (case (c))).

Adding short-wave and long-wave heating rates results in ~~SAL-net~~ SAL net heating rates that are entirely negative for both cases, taking values from -1.0 to -3.5 K d^{-1} (case (b)) and -0.5 to -5.5 K d^{-1} (case (c)). Moreover, an intensification of net radiative cooling with height towards the top of the SAL is evident.

Another increase in short-wave heating and long-wave cooling rates is found within the MBL which is characterized by a moist mixture of mineral dust and marine aerosols in all three cases. However, the shape of the MBL heating rate profile in SAL-influenced regions differs to those in SAL-free regions. While for the SAL-free scenario strong cooling at the top of the MBL can be observed (strongly pronounced MBL-inversion; case (a)), SAL-influenced regions show less cooling (weakly pronounced MBL-inversion; cases (b) and (c)). Short-wave, long-wave as well as net heating rate profiles calculated for the dust-free case (a) show no distinct features above the MBL. In this case peak values of atmospheric heating and cooling correlate with regions of strongest gradients in r_m (maximum long-wave cooling: -5 K d^{-1} ; maximum short-wave heating: 1.8 K d^{-1}). This emphasizes the dominating effect of water vapor on atmospheric heating.

3.3 SAL radiative effects at surface level and top of the atmosphere

Saharan dust short-wave radiative effects at surface level and TOA (Figure 5) are investigated by analyzing modeled solar zenith angle dependent short-wave irradiances for the three discussed scenarios. ~~It is assumed that the observed profiles do not change and remain stationary within a 24 h time frame.~~ Saharan dust short-wave radiative effects at surface level (RE_{SUR}) and top of

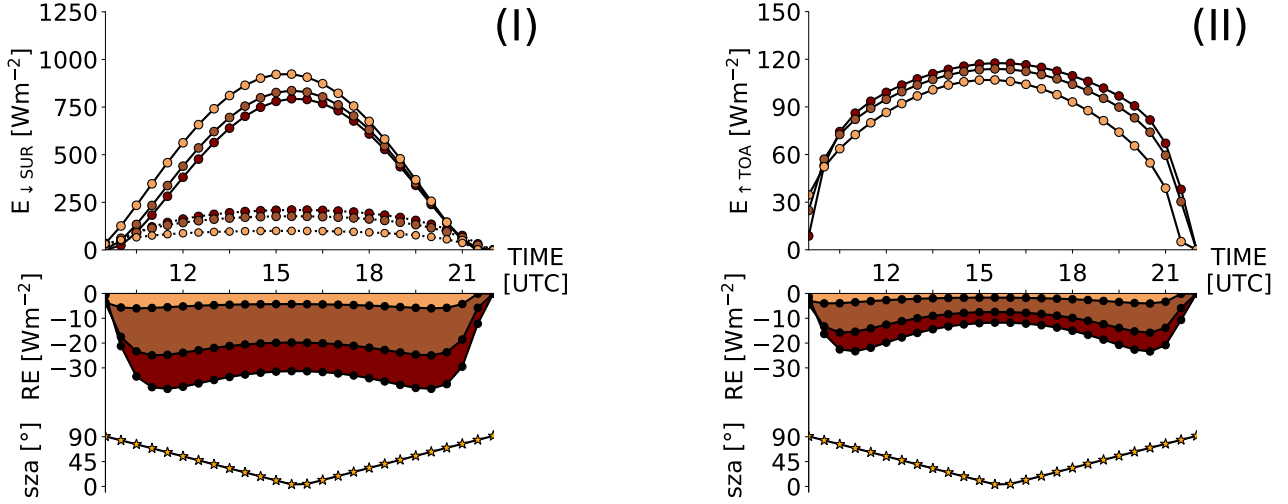


Figure 5. Top: Diurnal cycles of the modeled down-welling short-wave irradiances at surface level (I - $E_{\downarrow SUR}$: direct (solid), diffuse (dashed)) and up-welling short-wave irradiances at top of the atmosphere (II - $E_{\uparrow TOA}$). Due to the different measurement locations and small differences in corresponding solar zenith angles (sza) calculated curves are slightly shifted in x-direction. Bottom: The corresponding diurnal cycles of the modeled Saharan dust short-wave radiative effects (RE) at surface level (I) and top of the atmosphere (II). A representative sza for the whole measurement region is shown at the bottom ($11^{\circ} N$ and $55^{\circ} W$). Colors indicate the three cases: light-orange (case (a)), orange (case (b)), dark-orange (case (c)).

the atmosphere (RE_{TOA}) are inferred as the difference between modeled irradiances considering mineral dust particles in the model atmosphere ($E_{\downarrow tot}(SUR)$, $E_{\uparrow tot}(TOA)$) and irradiances calculated under assumption of no dust aerosol in the atmosphere ($E_{\downarrow nodust}(SUR)$, $E_{\uparrow nodust}(TOA)$),

$$RE_{SUR} = E_{\downarrow tot}(SUR) - E_{\downarrow nodust}(SUR). \quad (6)$$

5 and,

$$RE_{TOA} = -(E_{\uparrow tot}(TOA) - E_{\uparrow nodust}(TOA)), \quad (7)$$

[Water vapor distributions as measured by WALES are considered and included in the radiative transfer model setup.](#)

Downward and upward irradiances are primarily determined by solar elevation, therefore having a symmetrical shape with maxima at noon (around 15:30 UTC). The longer the slant path of solar rays through SALs, the more Mie- and Rayleigh-scattering processes and the larger the fraction of backscattered light to space. As a consequence, RE_{SUR} and RE_{TOA} show minimum magnitudes at low solar zenith angles around noon and maximum magnitudes at intermediate zenith angles in the morning and evening hours.

For case (c) ~~a maximum negative RE_{SUR} strongest radiative effects at surface level~~ of almost -40 W m^{-2} ~~is are~~ calculated for morning and evening hours (11:30 and 20:00 UTC). At noon the diffuse fraction of down-welling irradiance ($E_{\downarrow diff}$) at surface level reaches 200 W m^{-2} making one third of $E_{\downarrow tot}$ at surface levels. ~~Calculations of RE_{TOA} show similar results for case (e).~~ At intermediate zenith angles the diurnal ~~maximum maxima~~ in atmospheric backscattering ~~causes a maximum negative~~ ~~RE_{TOA} of -25 W m^{-2} also cause strongest radiative effects at TOA for case (c) (-25 W m^{-2}).~~ $E_{\uparrow tot}$ at TOA reaches maximum values of nearly 120 W m^{-2} at midday. For case (b) a lidar-derived RE_{SUR} of -25 W m^{-2} is computed for intermediate zenith angles. It ~~shows a local minimum weakens~~ at noon (~~-20 W m^{-2} -20 W m^{-2}~~). Compared to case (c), $E_{\downarrow diff}$ at noon is slightly smaller (180 W m^{-2}). This reduced diffuse fraction is also evident when looking at RE_{TOA} . Due to the decrease in scattering, ~~the magnitude of RE_{TOA} reduces to a minimum of -17 W m^{-2} is smaller than~~ for case (b) (-17 W m^{-2}). Compared to the other cases, case (a) shows the smallest ~~values magnitudes~~ of RE_{SUR} ($> -8 \text{ W m}^{-2}$) ~~with weakly pronounced maxima and strengthens only little~~ during sunrise and sunset. ~~RE_{TOA} is also weakest ($> -5 \text{ W m}^{-2}$) for case (a) is also the weakest ($> -5 \text{ W m}^{-2}$) when comparing all three cases.~~

4 Discussion

In this study the effects of mineral dust particles and water vapor on radiative heating rate profiles in SAL-influenced regions were studied. It was found, that the enhanced water vapor concentrations within the SALs cause a decrease of radiative heating rates towards the top of the SALs. This negative gradient with height is in agreement with results found by Kim et al. (2004) who focused on the effect of enhanced water vapor concentrations on atmospheric heating rates within Asian dust plumes. They ~~also highlighted that derived atmospheric compared heating rate calculations that include measured water vapor profiles to calculations that were performed using reference profiles. Their comparisons highlighted that~~ heating rates within the dust plumes are altered by enhanced water vapor concentrations ~~and compared heating rate calculations including measured water vapor profiles to reference profiles.~~ Calculated maximum short-wave heating and long-wave cooling rates were also found to be shifted from the center to the top of the dust layer when including the measured water vapor profile in their calculations. The strong negative trend of the heating rate profiles within the SALs is supposed to decrease the static stability in the layers and to promote vertical mixing and convective development. Vertical mixing in the SALs during their transport over the Atlantic Ocean was already proposed by Gasteiger et al. (2017) in an integrated study of active remote sensing, in-situ measurements and optical modeling. They suggested that vertical mixing within the SALs may counteract the Stokes gravitational settling during transport. Dropsonde measurements discussed in Section 3.1 confirm the well mixed and neutrally stratified layering in the interior of the SALs (~~$\Theta = \text{constant}$ $\Theta = \text{constant}$; $\Theta_e = \text{constant}$~~). It is bounded by inversions at the top and the bottom of the SALs (increase of net heating rates and positive changes of potential temperature), which separate the turbulent interior from the less turbulent free troposphere. An early model analysis by Lilly (1968) already suggested that these inversions are caused by radiative heating in SAL-altitudes.

Enhanced moisture inside the SAL also has an impact on the cooling and heating rate profile of the MBL. The dust-laden cases are found to show less infrared cooling at the top of the MBL compared to the SAL-free case. The elevated and moist SAL

is associated with down-welling long-wave irradiance which counteracts radiative cooling inside the MBL, thus weakening the cooling of the MBL. This leads to an almost homogeneous heating rate profile within the MBL. The SAL-free case in contrast indicates a negative heating rate gradient with strong negative heating rates at the top of the MBL. The nearly constant heating rate profile in the MBL counteracts convective development. Stevens et al. (2017) used idealized distributions of water vapor in the lower atmosphere to highlight the impact of elevated moist layers on the vertical distribution of heating rates. They claimed that such layers reduce the cooling at lower atmospheric levels and therefore modify the state of the boundary layer potentially inducing low-level circulations. A theoretical study by Naumann et al. (2017) already explained that variations in infrared cooling due to vertical gradients of tropospheric moisture may drive atmospheric circulations in trade wind regions. A correlation between long-range-transported elevated SAL and subjacent low-level cloudiness has been observed by Gutleben et al. (2019b). ~~Our~~Their analysis showed reduced cloud fractions and lower cloud top heights in trade wind regions comprising elevated mineral dust layers compared to dust-free regions. Moreover, observed dusty regions contained smaller clouds and showed greater cloud gaps than dust-laden regions.

Kanitz et al. (2013) studied the Saharan dust radiative effect at surface and TOA near source regions in the vicinity of the ~~Cap~~Cape Verde islands using shipborne aerosol Raman/polarization lidar measurements to parametrize the ~~atmospheres~~atmosphere's aerosol composition. Based on their lidar measurements on 1 May 2010 they deduced a maximum diurnal dust short-wave radiative effect of approximately -60 W m^{-2} at surface level and -42 W m^{-2} at TOA. These results are in good agreement with calculated radiative effects in this study. However, results in this paper are of a slightly smaller magnitude due to thinning of the SAL during long-range transport (-40 W m^{-2} at the surface and -25 W m^{-2} at TOA). ~~(Foltz and McPhaden, 2008)~~Foltz and McPhaden (2008) found that less down-welling solar radiation in dust-laden regions may cause gradients in sea surface temperature and potentially impacts the evolution of clouds in the MBL.

During NARVAL-II, the majority of mineral dust particles was always located above the MBL and inside the SAL. However, during previous field campaigns it was observed that the vertical distribution of long-range-transported mineral dust can be highly variable (Reid et al., 2002). During the Puerto Rico Dust Experiment (PRIDE) in summer 2000, for example, the majority of dust was in some cases observed to be located at lower atmospheric levels inside the MBL and in other cases it was observed to be located inside the SAL. A distinct seasonal pattern of Saharan dust transport towards the Atlantic Ocean was already found by Chiapello et al. (1995), who studied the vertical distribution of mineral dust particles at the beginning of long-range transport at the ~~Cap~~Cape Verde islands. They found that in contrast to the summer months, wintertime dust-transport towards the Atlantic Ocean is mainly taking place at lower atmospheric levels. ~~Questions regarding~~Furthermore, the observed vertical water vapor distribution during NARVAL-II may only be representative for an undisturbed SAL-transport during the summer months. Moisture originating from the outflow of the Intertropical convergence zone or from convective systems embedded in African Easterly Waves can modify the vertical moisture distribution in SAL-regions during disturbed transatlantic transports. Questions on the reasons for ~~these variable~~the variability in the vertical distributions of mineral dust and water vapor as well as whether there is a certain seasonal pattern in ~~the vertical distribution~~these vertical distributions not only at the beginning but also throughout the ~~long-range dust~~transatlantic transport can hopefully be answered in near future by analyzing data collected during the recent EUREC⁴A field campaign (Elucidating the Role of Clouds-Circulation Coupling

in ClimAte; Bony et al., 2017) in January 2020/February 2020. [An analysis of the EUREC⁴A data set will additionally provide valuable insights on the SAL-radiative effects during subtropical winter months.](#)

5 Summary and conclusions

This study investigated the effects of dust and water vapor in long-range-transported SALs on atmospheric heating rates and radiative transport on the basis of airborne lidar measurements over the western subtropical North Atlantic Ocean. Simultaneously measured profiles of water vapor mass mixing ratios and aerosol optical properties were used to characterize both the vertically resolved aerosol and water vapor composition in radiative transfer simulations.

Lidar measurements in Saharan dust-laden regions indicated enhanced concentrations of water vapor in SAL-altitudes and radiative transfer simulations revealed that water vapor plays the dominant role for atmospheric heating rates in these heights. Compared to water vapor, dust aerosol was identified to have a minor effect on total heating rates in SAL-altitudes showing small positive maximum heating rates of $0.3\text{--}0.5\text{ K d}^{-1}$ in the short-wave and slightly negative maximum cooling rates of -0.1 to -0.2 K d^{-1} in the long-wave spectrum at altitudes of highest aerosol mass concentration. Water vapor, however, was found to contribute much stronger to total SAL-heating rates with maximum short-wave and long-wave heating of $1.8\text{--}2.2\text{ K d}^{-1}$ and -6 K d^{-1} to -7 K d^{-1} at the uppermost levels of the SAL. As a result, calculated net heating rates inside SALs are entirely negative and decrease with altitude.

SALs were also found to have a possible impact on cloud development in the MBL. Besides possible impacts on low-level circulations, SALs introduce additional atmospheric counter-radiation towards the top of the MBL. As a result, MBL tops in dust-laden regions do not experience as much cooling as in SAL-free regions. This is also indicated by the heating rate profile in SAL-regions which is increasing with altitude and therefore counteracts the development of convection [in the MBL](#).

Last but not least, NARVAL-II lidar data were used to quantify the radiative effect of long-range-transported Saharan dust at surface level and top of the atmosphere. Maximum short-wave radiative effects of -40 W m^{-2} (surface) and 25 W m^{-2} (TOA) were found at intermediate zenith angles [for the presented case studies](#).

Summed up, radiative transfer calculations with NARVAL-II lidar data input highlighted the importance of correct representations of water vapor profiles in radiative transfer models and depicted the influence of mineral dust on the modification of solar irradiance throughout the atmosphere.

Data availability. The data used in this publication was collected during the NARVAL-II (Next-generation Aircraft Remote-Sensing for Validation Studies-II) campaign and is made available through the DLR Institute for Atmospheric Physics in the HALO database (German Aerospace Center, 2016; doi: 10.17616/R39Q0T).

Author contributions. In the framework of the NARVAL-II field experiment MW and SG contributed to carry out all airborne lidar measurements used in this study. MW did the initial data processing. MG performed the analytic computations, analyzed the dataset and performed

radiative transfer calculations with help BM and under supervision of SG. MG and SG took the lead in writing the manuscript. All authors discussed the results and contributed to the final manuscript.

Competing interests. The authors declare that they have no conflict of interest.

Acknowledgements. The authors like to thank the staff members of the DLR HALO aircraft from DLR Flight Experiments for preparing and performing the measurement flights. NARVAL-II was funded with support of the Max Planck Society, the German Research Foundation (DFG Priority Program: HALO-SSP 1294) and the German Aerospace Center (DLR). This study was funded by a DLR VO-R young investigator group within the Institute of Atmospheric Physics.

References

- Anderson, G. P., Clough, S. A., Kneizys, F. X., Chetwynd, J. H., and Shettle, E. P.: AFGL atmospheric constituent profiles (0-120 km), Tech. rep., 1986.
- Ansmann, A., Petzold, A., Kandler, K., Tegen, I., Wendisch, M., Müller, D., Weinzierl, B., Müller, T., and Heintzenberg, J.: Saharan
5 Mineral Dust Experiments SAMUM-1 and SAMUM-2: what have we learned?, *Tellus B*, 63, 403–429, <https://doi.org/10.1111/j.1600-0889.2011.00555.x>, 2011.
- Bellouin, N., Boucher, O., Vesperini, M., and Tanré, D.: Estimating the direct aerosol radiative perturbation: Impact of ocean surface representation and aerosol non-sphericity, *Q. J. Roy. Meteor. Soc.*, 130, 2217–2232, <https://doi.org/10.1256/qj.03.136>, 2004.
- Ben-Ami, Y., Koren, I., and Altaratz, O.: Patterns of North African dust transport over the Atlantic: winter vs. summer, based on CALIPSO
10 first year data, *Atmos. Chem. Phys.*, 9, 7867–7875, <https://doi.org/10.5194/acp-9-7867-2009>, 2009.
- Bony, S., Stevens, B., Ament, F., Bigorre, S., Chazette, P., Crewell, S., Delanoë, J., Emanuel, K., Farrell, D., Flamant, C., Groß, S., Hirsch, L., Karstensen, J., Mayer, B., Nuijens, L., Ruppert, J. H., Sandu, I., Siebesma, P., Speich, S., Szczap, F., Totems, J., Vogel, R., Wendisch, M., and Wirth, M.: EUREC4A: a field campaign to elucidate the couplings between clouds, convection and circulation, *Surv. Geophys.*, 38, 1529–1568, <https://doi.org/10.1007/s10712-017-9428-0>, 2017.
- 15 Buras, R., Dowling, T., and Emde, C.: New secondary-scattering correction in DISORT with increased efficiency for forward scattering, *J. Quant. Spectrosc. Ra.*, 112, 2028–2034, <https://doi.org/10.1016/j.jqsrt.2011.03.019>, 2011.
- Burton, S. P., Ferrare, R. A., Hostetler, C. A., Hair, J. W., Rogers, R. R., Obland, M. D., Butler, C. F., Cook, A. L., Harper, D. B., and Froyd, K. D.: Aerosol classification using airborne High Spectral Resolution Lidar measurements – methodology and examples, *Atmos. Meas. Tech.*, 5, 73–98, <https://doi.org/10.5194/amt-5-73-2012>, 2012.
- 20 Carlson, T. N. and Prospero, J. M.: The large-scale movement of Saharan air outbreaks over the northern equatorial Atlantic, *J. Appl. Meteorol.*, 11, 283–297, [https://doi.org/10.1175/1520-0450\(1972\)011<0283:TLSMOS>2.0.CO;2](https://doi.org/10.1175/1520-0450(1972)011<0283:TLSMOS>2.0.CO;2), 1972.
- Chiapello, I., Bergametti, G., Gomes, L., Chatenet, B., Dulac, F., Pimenta, J., and Soares, E. S.: An additional low layer transport of Sahelian and Saharan dust over the north-eastern Tropical Atlantic, *Geophys. Res. Lett.*, 22, 3191–3194, <https://doi.org/10.1029/95gl03313>, 1995.
- Claquin, T., Schulz, M., Balkanski, Y., and Boucher, O.: Uncertainties in assessing radiative forcing by mineral dust, *Tellus B*, 50, 491–505,
25 <https://doi.org/10.3402/tellusb.v50i5.16233>, 1998.
- Cox, C. and Munk, W.: Measurement of the roughness of the sea surface from photographs of the Sun’s glitter, *J. Opt. Soc. Am.*, 44, 838–850, <https://doi.org/10.1364/JOSA.44.000838>, 1954a.
- Cox, C. and Munk, W.: Statistics of the sea surface derived from Sun glitter, *J. Mar. Res.*, 13, 198–227, 1954b.
- Denjean, C., Caquineau, S., Desboeufs, K., Laurent, B., Maille, M., Rosado, M. Q., Vallejo, P., Mayol-Bracero, O. L., and Formenti, P.:
30 Long-range transport across the Atlantic in summertime does not enhance the hygroscopicity of African mineral dust, *Geophys. Re. Lett.*, 42, 7835–7843, <https://doi.org/10.1002/2015gl065693>, 2015.
- Emde, C., Buras-Schnell, R., Kylling, A., Mayer, B., Gasteiger, J., Hamann, U., Kylling, J., Richter, B., Pause, C., Dowling, T., and Bugliaro, L.: The libRadtran software package for radiative transfer calculations (version 2.0.1), *Geosci. Model Dev.*, 9, 1647–1672, <https://doi.org/10.5194/gmd-9-1647-2016>, 2016.
- 35 Esselborn, M., Wirth, M., Fix, A., Tesche, M., and Ehret, G.: Airborne high spectral resolution lidar for measuring aerosol extinction and backscatter coefficients, *Appl. Opt.*, 47, 346–358, <https://doi.org/10.1364/AO.47.000346>, 2008.

- Ewald, F., Kölling, T., Baumgartner, A., Zinner, T., and Mayer, B.: Design and characterization of specMACS, a multipurpose hyperspectral cloud and sky imager, *Atmos. Meas. Tech.*, 9, 2015–2042, <https://doi.org/10.5194/amt-9-2015-2016>, 2016.
- Ewald, F., Groß, S., Hagen, M., Hirsch, L., Delanoë, J., and Bauer-Pfundstein, M.: Calibration of a 35 GHz airborne cloud radar: lessons learned and intercomparisons with 94 GHz cloud radars, *Atmos. Meas. Tech.*, 12, 1815–1839, <https://doi.org/10.5194/amt-12-1815-2019>, 2019.
- 5 Falkovich, A. H., Ganor, E., Levin, Z., Formenti, P., and Rudich, Y.: Chemical and mineralogical analysis of individual mineral dust particles, *J. Geophys. Res.-Atmos.*, 106, 18 029–18 036, <https://doi.org/10.1029/2000jd900430>, 2001.
- Foltz, G. R. and McPhaden, M. J.: Impact of Saharan dust on tropical North Atlantic SST, *J. Climate*, 21, 5048–5060, <https://doi.org/10.1175/2008jcli2232.1>, 2008.
- 10 Freudenthaler, V., Esselborn, M., Wiegner, M., Heese, B., Tesche, M., Ansmann, A., Müller, D., Althausen, D., Wirth, M., Fix, A., Ehret, G., Knippertz, P., Toledano, C., Gasteiger, J., Garhammer, M., and Seefeldner, M.: Depolarization ratio profiling at several wavelengths in pure Saharan dust during SAMUM 2006, *Tellus B*, 61, 165–179, <https://doi.org/10.1111/j.1600-0889.2008.00396.x>, 2009.
- Fu, Q. and Liou, K. N.: On the correlated k-distribution method for radiative transfer in nonhomogeneous atmospheres, *J. Atmos. Sci.*, 49, 2139–2156, [https://doi.org/10.1175/1520-0469\(1992\)049<2139:OTCDMF>2.0.CO;2](https://doi.org/10.1175/1520-0469(1992)049<2139:OTCDMF>2.0.CO;2), 1992.
- 15 Gasteiger, J., Wiegner, M., Groß, S., Freudenthaler, V., Toledano, C., Tesche, M., and Kandler, K.: Modelling lidar-relevant optical properties of complex mineral dust aerosols, *Tellus B*, 63, 725–741, <https://doi.org/10.1111/j.1600-0889.2011.00559.x>, 2011.
- Gasteiger, J., Groß, S., Sauer, D., Haarig, M., Ansmann, A., and Weinzierl, B.: Particle settling and vertical mixing in the Saharan Air Layer as seen from an integrated model, lidar, and in situ perspective, *Atmos. Chem. Phys.*, 17, 297–311, <https://doi.org/10.5194/acp-17-297-2017>, 2017.
- 20 German Aerospace Center: <https://doi.org/10.17616/R39Q0T>, 2016.
- Gobbi, G., Barnaba, F., Blumthaler, M., Labow, G., and Herman, J.: Observed effects of particles nonsphericity on the retrieval of marine and desert dust aerosol optical depth by lidar, *Atmos. Res.*, 61, 1–14, [https://doi.org/10.1016/s0169-8095\(01\)00104-1](https://doi.org/10.1016/s0169-8095(01)00104-1), 2002.
- Groß, S., Tesche, M., Freudenthaler, V., Toledano, C., Wiegner, M., Ansmann, A., Althausen, D., and Seefeldner, M.: Characterization of Saharan dust, marine aerosols and mixtures of biomass-burning aerosols and dust by means of multi-wavelength depolarization and Raman
- 25 lidar measurements during SAMUM 2, *Tellus B*, 63, 706–724, <https://doi.org/10.1111/j.1600-0889.2011.00556.x>, 2011a.
- Groß, S., Wiegner, M., Freudenthaler, V., and Toledano, C.: Lidar ratio of Saharan dust over Cape Verde Islands: Assessment and error calculation, *J. Geophys. Res.-Atmos.*, 116, <https://doi.org/10.1029/2010JD015435>, d15203, 2011b.
- Groß, S., Esselborn, M., Weinzierl, B., Wirth, M., Fix, A., and Petzold, A.: Aerosol classification by airborne high spectral resolution lidar observations, *Atmos. Chem. Phys.*, 13, 2487–2505, <https://doi.org/10.5194/acp-13-2487-2013>, 2013.
- 30 Groß, S., Freudenthaler, V., Schepanski, K., Toledano, C., Schäfler, A., Ansmann, A., and Weinzierl, B.: Optical properties of long-range transported Saharan dust over Barbados as measured by dual-wavelength depolarization Raman lidar measurements, *Atmos. Chem. Phys.*, 15, 11 067–11 080, <https://doi.org/10.5194/acp-15-11067-2015>, 2015.
- Groß, S., Gasteiger, J., Freudenthaler, V., Müller, T., Sauer, D., Toledano, C., and Ansmann, A.: Saharan dust contribution to the Caribbean summertime boundary layer – a lidar study during SALTRACE, *Atmos. Chem. Phys.*, 16, 11 535–11 546, <https://doi.org/10.5194/acp-16-11535-2016>, 2016.
- 35 Gutleben, M., Groß, S., Wirth, M., Emde, C., and Mayer, B.: Impacts of water vapor on Saharan Air Layer radiative heating, *Geophys. Res. Lett.*, 46, 14 854–14 862, <https://doi.org/10.1029/2019GL085344>, 2019a.

- Gutleben, M., Groß, S., and Wirth, M.: Cloud macro-physical properties in Saharan-dust-laden and dust-free North Atlantic trade wind regimes: a lidar case study, *Atmos. Chem. Phys.*, 19, 10 659–10 673, <https://doi.org/10.5194/acp-19-10659-2019>, 2019b.
- Haarig, M., Ansmann, A., Althausen, D., Klepel, A., Groß, S., Freudenthaler, V., Toledano, C., Mamouri, R.-E., Farrell, D. A., Prescod, D. A., Marinou, E., Burton, S. P., Gasteiger, J., Engelmann, R., and Baars, H.: Triple-wavelength depolarization-ratio profiling of Saharan dust over Barbados during SALTRACE in 2013 and 2014, *Atmos. Chem. Phys.*, 17, 10 767–10 794, <https://doi.org/10.5194/acp-17-10767-2017>, 2017a.
- Haarig, M., Ansmann, A., Gasteiger, J., Kandler, K., Althausen, D., Baars, H., Radenz, M., and Farrell, D. A.: Dry versus wet marine particle optical properties: RH dependence of depolarization ratio, backscatter, and extinction from multiwavelength lidar measurements during SALTRACE, *Atmos. Chem. Phys.*, 17, 14 199–14 217, <https://doi.org/10.5194/acp-17-14199-2017>, 2017b.
- 10 Hess, M., Koepke, P., and Schult, I.: Optical Properties of Aerosols and Clouds: the software package OPAC, *B. Am. Meteorol. Soc.*, 79, 831–844, [https://doi.org/10.1175/1520-0477\(1998\)079<0831:opoaac>2.0.co;2](https://doi.org/10.1175/1520-0477(1998)079<0831:opoaac>2.0.co;2), 1998.
- Jung, E., Albrecht, B., Prospero, J. M., Jonsson, H. H., and Kreidenweis, S. M.: Vertical structure of aerosols, temperature, and moisture associated with an intense African dust event observed over the eastern Caribbean, *J. Geophys. Res.-Atmospheres*, 118, 4623–4643, <https://doi.org/10.1002/jgrd.50352>, 2013.
- 15 Kaaden, N., Massling, A., Schladitz, A., Müller, T., Kandler, K., Schütz, L., Weinzierl, B., Petzold, A., Tesche, M., Leinert, S., Deutscher, C., Ebert, M., Weinbruch, S., and Wiedensohler, A.: State of mixing, shape factor, number size distribution, and hygroscopic growth of the Saharan anthropogenic and mineral dust aerosol at Tinfou, Morocco, *Tellus B*, 61, 51–63, <https://doi.org/10.1111/j.1600-0889.2008.00388.x>, 2009.
- Kahnert, M., Nousianen, T., and Veihelmann, B.: Spherical and spheroidal model particles as an error source in aerosol climate forcing and radiance computations: A case study for feldspar aerosols, *J. Geophys. Res.-Atmospheres*, 110, <https://doi.org/10.1029/2004jd005558>, 2005.
- 20 Kandler, K., Schütz, L., Deutscher, C., Ebert, M., Hofmann, H., Jäckel, S., Jaenicke, R., Knippertz, P., Lieke, K., Massling, A., Petzold, A., Schladitz, A., Weinzierl, B., Wiedensohler, A., Zorn, S., and Weinbruch, S.: Size distribution, mass concentration, chemical and mineralogical composition and derived optical parameters of the boundary layer aerosol at Tinfou, Morocco, during SAMUM 2006, *Tellus B*, 61, 32–50, <https://doi.org/10.1111/j.1600-0889.2008.00385.x>, 2009.
- 25 Kandler, K., Lieke, K., Benker, N., Emmel, C., Küpper, M., Müller-Ebert, D., Ebert, M., Scheuven, D., Schladitz, A., Schütz, L., and Weinbruch, S.: Electron microscopy of particles collected at Praia, Cape Verde, during the Saharan Mineral Dust Experiment: particle chemistry, shape, mixing state and complex refractive index, *Tellus B*, 63, 475–496, <https://doi.org/10.1111/j.1600-0889.2011.00550.x>, 2011.
- 30 Kanitz, T., Ansmann, A., Seifert, P., Engelmann, R., Kalisch, J., and Althausen, D.: Radiative effect of aerosols above the northern and southern Atlantic Ocean as determined from shipborne lidar observations, *J. Geophys. Res.-Atmos.*, 118, 12,556–12,565, <https://doi.org/10.1002/2013jd019750>, 2013.
- Kanitz, T., Engelmann, R., Heinold, B., Baars, H., Skupin, A., and Ansmann, A.: Tracking the Saharan Air Layer with shipborne lidar across the tropical Atlantic, *Geophys. Res. Lett.*, 41, 1044–1050, <https://doi.org/10.1002/2013gl058780>, 2014.
- 35 Karyampudi, V. M. and Carlson, T. N.: Analysis and numerical simulations of the Saharan air layer and its effect on easterly wave disturbances, *J. Atmos. Sci.*, 45, 3102–3136, 1988.

- Karyampudi, V. M., Palm, S. P., Reagen, J. A., Fang, H., Grant, W. B., Hoff, R. M., Moulin, C., Pierce, H. F., Torres, O., Browell, E. V., and Melfi, S. H.: Validation of the Saharan dust plume conceptual model using lidar, Meteosat, and ECMWF data, *B. Am. Meteorol. Soc.*, 80, 1045–1075, [https://doi.org/10.1175/1520-0477\(1999\)080<1045:VOTSDP>2.0.CO;2](https://doi.org/10.1175/1520-0477(1999)080<1045:VOTSDP>2.0.CO;2), 1999.
- 5 Kato, S., Ackerman, T. P., Mather, J. H., and Clothiaux, E. E.: The k-distribution method and correlated-k approximation for a shortwave radiative transfer model, *J. Quant. Spectrosc. Ra.*, 62, 109–121, [https://doi.org/10.1016/s0022-4073\(98\)00075-2](https://doi.org/10.1016/s0022-4073(98)00075-2), 1999.
- Kiemle, C., Wirth, M., Fix, A., Ehret, G., Schumann, U., Gardiner, T., Schiller, C., Sitnikov, N., and Stiller, G.: First airborne water vapor lidar measurements in the tropical upper troposphere and mid-latitudes lower stratosphere: accuracy evaluation and intercomparisons with other instruments, *Atmos. Chem. Phys.*, 8, 5245–5261, <https://doi.org/10.5194/acp-8-5245-2008>, 2008.
- 10 Kim, S., Yoon, S., Jefferson, A., Won, J., Dutton, E. G., Ogren, J. A., and Anderson, T. L.: Observation of enhanced water vapor in Asian dust layer and its effect on atmospheric radiative heating rates, *Geophys. Res. Lett.*, 31, <https://doi.org/10.1029/2004gl020024>, 2004.
- Koepke, P. and Hess, M.: Scattering functions of tropospheric aerosols: the effects of nonspherical particles, *Appl. Opt.*, 27, 2422, <https://doi.org/10.1364/ao.27.002422>, 1988.
- Koepke, P., Gasteiger, J., and Hess, M.: Technical Note: Optical properties of desert aerosol with non-spherical mineral particles: data incorporated to OPAC, *Atmos. Chem. Phys.*, 15, 5947–5956, <https://doi.org/10.5194/acp-15-5947-2015>, 2015.
- 15 Krautstrunk, M. and Giez, A.: The transition from FALCON to HALO era airborne atmospheric research, in: *Atmospheric Physics*, edited by Schumann, U., *Research Topics in Aerospace*, pp. 609–624, Springer Berlin Heidelberg, 2012.
- Li, F., Vogelmann, A. M., and Ramanathan, V.: Saharan dust aerosol radiative forcing measured from space, *J. Climate*, 17, 2558–2571, [https://doi.org/10.1175/1520-0442\(2004\)017<2558:sdarfm>2.0.co;2](https://doi.org/10.1175/1520-0442(2004)017<2558:sdarfm>2.0.co;2), 2004.
- Liao, H. and Seinfeld, J. H.: Radiative forcing by mineral dust aerosols: sensitivity to key variables, *J. Geophys. Res.-Atmos.*, 103, 31 637–20 31 645, <https://doi.org/10.1029/1998JD200036>, 1998.
- Lilly, D. K.: Models of cloud-topped mixed layers under a strong inversion, *Q. J. Roy. Meteor. Soc.*, 94, 292–309, <https://doi.org/10.1002/qj.49709440106>, 1968.
- Liu, Z., Vaughan, M. A., Winker, D. M., Hostetler, C. A., Poole, L. R., Hlavka, D., Hart, W., and M., M.: Use of probability distribution functions for discriminating between cloud and aerosol in lidar backscatter data, *J. Geophys. Res.*, 109, <https://doi.org/10.1029/2004jd004732>, 25 2004.
- Mamouri, R.-E. and Ansmann, A.: Potential of polarization lidar to provide profiles of CCN- and INP-relevant aerosol parameters, *Atmos. Chem. Phys.*, 16, 5905–5931, <https://doi.org/10.5194/acp-16-5905-2016>, 2016.
- Mayer, B. and Kylling, A.: Technical note: The libRadtran software package for radiative transfer calculations - description and examples of use, *Atmos. Chem. Phys.*, 5, 1855–1877, <https://doi.org/10.5194/acp-5-1855-2005>, 2005.
- 30 Mech, M., Orlandi, E., Crewell, S., Ament, F., Hirsch, L., Hagen, M., Peters, G., and Stevens, B.: HAMP – the microwave package on the High Altitude and Long range research aircraft (HALO), *Atmos. Meas. Tech.*, 7, 4539–4553, <https://doi.org/10.5194/amt-7-4539-2014>, 2014.
- Mie, G.: Beiträge zur Optik trüber Medien, speziell kolloidaler Metallösungen, *Ann. Phys.*, 330, 377–445, <https://doi.org/10.1002/andp.19083300302>, 1908.
- 35 Mishchenko, M. I., Travis, L. D., Kahn, R. A., and West, R. A.: Modeling phase functions for dustlike tropospheric aerosols using a shape mixture of randomly oriented polydisperse spheroids, *J. Geophys. Res.-Atmos.*, 102, 16 831–16 847, <https://doi.org/10.1029/96jd02110>, 1997.

- Moulin, C., Lambert, C. E., Dulac, F., and Dayan, U.: Control of atmospheric export of dust from North Africa by the North Atlantic Oscillation, *Nature*, 387, 691–694, <https://doi.org/10.1038/42679>, 1997.
- Murayama, T., Okamoto, H., Kaneyasu, N., Kamataki, H., and Miura, K.: Application of lidar depolarization measurement in the atmospheric boundary layer: effects of dust and sea-salt particles, *J. Geophys. Res.-Atmos.*, 104, 31 781–31 792, <https://doi.org/10.1029/1999jd900503>, 5 1999.
- Naumann, A. K., Stevens, B., Hohenegger, C., and Mellado, J. P.: A conceptual model of a shallow circulation induced by prescribed low-level radiative cooling, *J. Atmos. Sci.*, 74, 3129–3144, <https://doi.org/10.1175/jas-d-17-0030.1>, 2017.
- Nousiainen, T.: Optical modeling of mineral dust particles: a review, *J. Quant. Spectrosc. Ra.*, 110, 1261–1279, <https://doi.org/10.1016/j.jqsrt.2009.03.002>, 2009.
- 10 Patadia, F., Yang, E.-S., and Christopher, S. A.: Does dust change the clear sky top of atmosphere shortwave flux over high surface reflectance regions?, *Geophys. Res. Lett.*, 36, <https://doi.org/10.1029/2009gl039092>, 2009.
- Prospero, J. M. and Carlson, T. N.: Vertical and areal distribution of Saharan dust over the western equatorial North Atlantic Ocean, *J. Geophys. Res.*, 77, 5255–5265, <https://doi.org/10.1029/JC077i027p05255>, 1972.
- Reid, J. S., Westphal, D. L., Livingston, J. M., Savoie, D. L., Maring, H. B., Jonsson, H. H., Eleuterio, D. P., Kinney, J. E., 15 and Reid, E. A.: Dust vertical distribution in the Caribbean during the Puerto Rico Dust Experiment, *Geophys. Res. Lett.*, 29, <https://doi.org/10.1029/2001gl014092>, 2002.
- Sakai, T., Nagai, T., Zaizen, Y., and Mano, Y.: Backscattering linear depolarization ratio measurements of mineral, sea-salt, and ammonium sulfate particles simulated in a laboratory chamber, *Appl. Opt.*, 49, 4441, <https://doi.org/10.1364/ao.49.004441>, 2010.
- Sakai, T., Orikasa, N., Nagai, T., Murakami, M., Tajiri, T., Saito, A., Yamashita, K., and Hashimoto, A.: Balloon-borne and Ra- 20 man lidar observations of Asian dust and cirrus cloud properties over Tsukuba, Japan, *J. Geophys. Res.-Atmos.*, 119, 3295–3308, <https://doi.org/10.1002/2013jd020987>, 2014.
- Schepanski, K., Tegen, I., Todd, M. C., Heinold, B., Bönisch, G., Laurent, B., and Macke, A.: Meteorological processes forcing Saharan dust emission inferred from MSG-SEVIRI observations of subdaily dust source activation and numerical models, *J. Geophys. Res.*, 114, <https://doi.org/10.1029/2008jd010325>, 2009.
- 25 Stamnes, K., Tsay, S.-C., Wiscombe, W., and Jayaweera, K.: Numerically stable algorithm for discrete-ordinate-method radiative transfer in multiple scattering and emitting layered media, *Appl. Opt.*, 27, 2502, <https://doi.org/10.1364/ao.27.002502>, 1988.
- Stein, A. F., Draxler, R. R., Rolph, G. D., Stunder, B. J. B., Cohen, M. D., and Ngan, F.: NOAA’s HYSPLIT atmospheric transport and dispersion modeling system, *B. Am. Meteorol. Soc.*, 96, 2059–2077, <https://doi.org/10.1175/BAMS-D-14-00110.1>, 2015.
- Stevens, B., Brogniez, H., Kiemle, C., Lacour, J.-L., Crevoisier, C., and Kiliani, J.: Structure and dynamical influence of water vapor in the 30 lower tropical troposphere, *Surv. Geophys.*, 38, 1371–1397, <https://doi.org/10.1007/s10712-017-9420-8>, 2017.
- Stevens, B., Ament, F., Bony, S., Crewell, S., Ewald, F., Groß, S., Hansen, A., Hirsch, L., Jacob, M., Kölling, T., Konow, H., Mayer, B., Wendisch, M., Wirth, M., Wolf, K., Bakan, S., Bauer-Pfundstein, M., Brueck, M., Delanoë, J., Ehrlich, A., Farrell, D., Forde, M., Gödde, F., Grob, H., Hagen, M., Jäkel, E., Jansen, F., Klepp, C., Klingebiel, M., Mech, M., Peters, G., Rapp, M., Wing, A. A., and Zinner, T.: A high-altitude long-range aircraft configured as a cloud observatory - the NARVAL expeditions, *B. Am. Meteorol. Soc.*, 35 <https://doi.org/10.1175/bams-d-18-0198.1>, 2019.
- Tesche, M., Ansmann, A., Müller, D., Althausen, D., Engelmann, R., Freudenthaler, V., and Groß, S.: Vertically resolved separation of dust and smoke over Cape Verde using multiwavelength Raman and polarization lidars during Saharan Mineral Dust Experiment 2008, *J. Geophys. Res.*, 114, <https://doi.org/10.1029/2009jd011862>, 2009a.

- Tesche, M., Ansmann, A., Müller, D., Althausen, D., Mattis, I., Heese, B., Freudenthaler, V., Wiegner, M., Esselborn, M., Pisani, G., and Knippertz, P.: Vertical profiling of Saharan dust with Raman lidars and airborne HSRL in southern Morocco during SAMUM, *Tellus B*, 61, 144–164, <https://doi.org/10.1111/j.1600-0889.2008.00390.x>, 2009b.
- Toledano, C., Torres, B., Velasco-Merino, C., Althausen, D., Groß, S., Wiegner, M., Weinzierl, B., Gasteiger, J., Ansmann, A., González, R., 5 Mateos, D., Farrel, D., Müller, T., Haarig, M., and Cachorro, V. E.: Sun photometer retrievals of Saharan dust properties over Barbados during SALTRACE, *Atmos. Chem. Phys.*, 19, 14 571–14 583, <https://doi.org/10.5194/acp-19-14571-2019>, 2019.
- Waterman, P. C.: Symmetry, unitarity, and geometry in electromagnetic scattering, *Phys. Rev. D*, 3, 825–839, <https://doi.org/10.1103/PhysRevD.3.825>, 1971.
- Weinzierl, B., Ansmann, A., Prospero, J. M., Althausen, D., Benker, N., Chouza, F., Dollner, M., Farrell, D., Fomba, W. K., Freudenthaler, V., 10 Gasteiger, J., Groß, S., Haarig, M., Heinold, B., Kandler, K., Kristensen, T. B., Mayol-Bracero, O. L., Müller, T., Reitebuch, O., Sauer, D., Schäfler, A., Schepanski, K., Spanu, A., Tegen, I., Toledano, C., and Walser, A.: The Saharan Aerosol Long-Range Transport and Aerosol-Cloud-Interaction Experiment: overview and selected highlights, *B. Am. Meteorol. Soc.*, 98, 1427–1451, <https://doi.org/10.1175/BAMS-D-15-00142.1>, 2017.
- Wendisch, M., Müller, D., Schell, D., and Heintzenberg, J.: An airborne spectral albedometer with active horizontal stabilization, *J. Atmos. 15 Ocean. Tech.*, 18, 1856–1866, [https://doi.org/10.1175/1520-0426\(2001\)018<1856:aasawa>2.0.co;2](https://doi.org/10.1175/1520-0426(2001)018<1856:aasawa>2.0.co;2), 2001.
- Wiegner, M., Gasteiger, J., Kandler, K., Weinzierl, B., Rasp, K., Esselborn, M., Freudenthaler, V., Heese, B., Toledano, C., Tesche, M., and Althausen, D.: Numerical simulations of optical properties of Saharan dust aerosols with emphasis on lidar applications, *Tellus B*, 61, 180–194, <https://doi.org/10.1111/j.1600-0889.2008.00381.x>, 2009.
- Wirth, M., Fix, A., Mahnke, P., Schwarzer, H., Schrandt, F., and Ehret, G.: The airborne multi-wavelength water vapor differential absorption 20 lidar WALES: system design and performance, *Appl. Phys. B*, 96, 201–213, <https://doi.org/10.1007/s00340-009-3365-7>, 2009.
- Wong, S. and Dessler, A. E.: Suppression of deep convection over the tropical North Atlantic by the Saharan Air Layer, *Geophys. Res. Lett.*, 32, <https://doi.org/10.1029/2004gl022295>, 2005.
- Wong, S., Dessler, A. E., Mahowald, N. M., Yang, P., and Feng, Q.: Maintenance of lower tropospheric temperature inversion in the Saharan Air Layer by dust and dry anomaly, *J. Clim.*, 22, 5149–5162, <https://doi.org/10.1175/2009jcli2847.1>, 2009.
- 25 Yi, B., Hsu, C. N., Yang, P., and Tsay, S.-C.: Radiative transfer simulation of dust-like aerosols: uncertainties from particle shape and refractive index, *J. Aerosol Sci.*, 42, 631–644, <https://doi.org/10.1016/j.jaerosci.2011.06.008>, 2011.
- Zhu, A., Ramanathan, V., Li, F., and Kim, D.: Dust plumes over the Pacific, Indian, and Atlantic oceans: climatology and radiative impact, *J. Geophys. Res.*, 112, <https://doi.org/10.1029/2007jd008427>, 2007.